HST OBSERVATIONS OF NEARBY RADIO-LOUD EARLY-TYPE GALAXIES[1]

Gijs A. Verdoes Kleijn,[2,3] Stefi A. Baum,[3] P. Tim de Zeeuw,[2] Chris P. O'Dea[3]

[1]Based on observations with the NASA/ESA Hubble Space Telescope obtained at the Space Telescope Science Institute, which is operated by the Association of Universities for Research in Astronomy, Incorporated, under NASA contract NAS5-26555.

[2]Sterrewacht Leiden, Postbus 9513, 2300 RA Leiden, The Netherlands.

[3]Space Telescope Science Institute, 3700 San Martin Drive, Baltimore, MD 21218.

ABSTRACT

We present and analyse HST/WFPC2 broad- and narrow-band observations of the central regions of 19 nearby radio-loud early-type galaxies. Together with two more galaxies they form a complete sample of Fanaroff & Riley Type I galaxies. We obtained V- and I-band images and narrow-band images centered on the Hα+[NII] emission lines. We use archival data for six galaxies.

We describe the data reduction, give isophotal fits and analyse the central emission-line gas and dust distributions. Our main conclusions are the following. Although obscuration by dust inhibits a direct determination of central cusp slopes, the data suggest most but not all galaxies have shallow cores. Dust is detected in all but two galaxies. There is a wide variety of central dust morphologies, ranging from central disks to lanes and irregular distributions. The analysis suggests the difference between disks and lanes is intrinsic and not due to different viewing angles. Central emission-line gas is detected in all galaxies. Extended low-surface-brightness emission is always associated with the dust features. In a subsequent paper we will present a detailed analysis of the relation between these central properties and the nuclear activity.

Subject headings: galaxies: active — galaxies: elliptical and lenticular, cD — ISM: dust, extinction

1. INTRODUCTION

Galaxies with radio jets are enigmatic objects. The sizes of the radio jets can reach up to ~ 1 Mpc. Yet the central 'engine' which powers the radio jets resides at the center of the galaxy in an active region $\sim 10^{-3}$ pc in radius: the spatially unresolved AGN. The energy for the huge radio jets (with luminosities as large as 10^{38} W between 10 MHz and 100 GHz) is generally believed to be produced by the accretion of matter onto a central super-massive black hole (hereafter BH) (e.g., Rees 1984; see Lynden-Bell 1996 for a historical overview). This view is supported e.g. by short time-scale variability of the central X-ray sources detected in active galaxies (e.g., Wagner and Witzel 1995 for a review), and by the detection of super-massive black holes in several nearby active and normal galaxies (e.g., Ford et al. 1998; Ho 1998; Richstone 1998; van der Marel 1998 for summaries and reviews of recent results). Within this paradigm there remain many fundamental unanswered questions concerning the formation and evolution of AGN in radio-loud galaxies. For instance, what triggers the formation of a radio jet? Why are powerful radio jets always found in early-type galaxies rather than in spirals? Why do we see radio jets only in a few percent of early-type galaxies? What is the origin of the material falling on to the BH? Is it obtained from the host galaxy itself or is it obtained by merging or galaxy harassment? What is the 'feeding' mechanism of the massive BH: how did the accreted material loose its angular momentum? And finally, what causes the collimation of the jets?

Radio emission is observed from the cores of a considerable fraction (at least 20% at $M_B = -19.5$ and 50% at $M_B = -22$) of all early-type galaxies (e.g., Sadler 1997 and references therein). Only a few of these galaxies also show radio jets. Ground-based studies of nearby galaxies with radio jets have shown that they are predominantly ellipticals with luminosity $\geq L_*$ (e.g., Owen and Laing 1989). They tend to be less flattened than normal galaxies (Hummel et al. 1983; Disney et al. 1984), and tend to have boxy isophotes (Bender et al. 1989). At equal luminosity, S0 galaxies are a factor ten weaker radio emitters than elliptical galaxies (Hummel & Kotanyi 1982; Cordey 1986). Radio-loud early-type galaxies show dust more than twice as often than their normal counterparts (van Dokkum & Franx 1995). The dust distributions appear to be broadly perpendicular to the radio jet axis (Kotanyi & Ekers 1979; de Koff et al. 1999).

With the advent of `HST` the central regions of galaxies have been studied in the optical with unprecedented high resolution. Studies of samples of nearby normal dust-free ellipticals reported a dichotomy in the types of central surface brightness profiles (e.g., Jaffe et al. 1994; Lauer et al. 1995). Some galaxies have surface brightness profiles, $I(r) \sim r^{-\gamma}$, with $\gamma > 0.5$ (i.e., a steep cusp) while others have profiles with $\gamma < 0.3$ (i.e., a shallow cusp). High-luminosity galaxies ($M_B \leq -21.5$) predominantly have shallow cusps while lower luminosity galaxies predominantly have steep central cusps. However, a study of the nuclei of ellipticals with counter rotating cores (Carollo et al. 1997) suggests a rather smooth transition zone between the two classes instead of a bimodal distribution. The central regions of both normal and radio-loud galaxies turned out to be a diverse and complex environment. Small nuclear gas and dust disks with sizes of a few hundred parsec were discovered in several galaxies (Jaffe et al. 1993; De Juan et al. 1996; Baum et al. 1997; van der Marel & van den Bosch 1998; de Koff et al. 1999). The central gas disks in M 87 (Ford et al. 1994) and M 84 (Bower et al. 1997) were studied in detail. They both lie in an irregular dust

and gas distribution already known from ground-based work (e.g., Kormendy & Stauffer 1987). Super-massive BHs were detected by modeling the kinematics of the nuclear emission-line disks in M 87 (Harms et al. 1994), NGC 4261 (Ferrarese et al. 1996), M 84 (Bower et al. 1998) and NGC 7052 (van der Marel & van den Bosch 1998). Previously unknown optical jets were detected in several nearby radio-loud galaxies (e.g., Sparks et al. 1994; Baum et al. 1997, Martel et al. 1998).

BH masses display a roughly linear correlation with total luminosity of the host bulge (Kormendy & Richstone 1995; van der Marel 1998), but there is an observational bias against detecting small BHs in big galaxies, as well as a large scatter at fixed luminosity. The absolute magnitude for the four nearby radio-loud galaxies in which BHs were found varies by only 0.2 while their BH masses differ by a factor ~ 10 and their radio power varies by a factor ~ 70.

Given the HST results for nearby normal galaxies and the variety of features observed in radio galaxies, it is important to survey the central regions of nearby radio-loud galaxies in a systematic and unbiased way. How do the central regions of radio-loud early-types differ from the central regions of their radio-quiet and normal counterparts? What is the range of inner slopes of the luminosity profiles? Are there 'reservoirs' of matter such as disks of gas and dust in all radio-loud galaxies? How do the properties of the dust and gas distributions, such as mass, kinematics and orientation, correlate with the properties of the radio jets? How do the inner radio jets and the central interstellar medium (hereafter ISM) interact? What is the relation between optical luminosity, radio luminosity and BH mass for radio-loud galaxies?

Answers to the above questions require a systematic and observationally unbiased approach. Therefore we defined a complete sample of 21 nearby radio-loud early-type galaxies limited in radio-flux and redshift (see Sec. 2.1). We carried out a program to obtain images for 19 galaxies. For six of those galaxies we use archival HST data. We obtained broad-band V and I images to study the central light distributions, color and the distribution of dust. We also obtained narrow-band images centered on the Hα+[NII] emission lines to probe the emission gas at the centers of these galaxies.

The purpose of this paper is to present the sample and the observations, to describe in detail the data reduction and to give a preliminary analysis of the dust and gas emission for the 19 galaxies. In a subsequent paper we will present a detailed analysis of the properties of the centers of these galaxies and their relation to the nuclear activity. Studies of the same sample at radio and X-ray frequencies are described in Xu et al. (1999a,b).

The paper is organized as follows. In Sec. 2 we introduce the sample and describe the observations and reduction of the images. We discuss the procedure and results for the isophotal analysis in Sec. 3, for the emission gas analysis in Sec. 4 and for the dust analysis in Sec. 5. A summary of the results and conclusions is given in Sec 6. A description for the individual galaxies is given in Appendix A and details on the derivation of optical depths is given in Appendix B.

Throughout the paper we use a Hubble constant H_0= 75 kms^{-1}Mpc^{-1}.

2. OBSERVATIONS AND IMAGE DATA REDUCTION

2.1. The Sample

Our objective was to select a well-defined complete sample of nearby galaxies with radio jets to study in a systematic way and with high spatial resolution their central properties. The complete sample is drawn from a catalog of 176 radio-loud galaxies constructed by Condon & Broderick (1988, hereafter CB88). The catalog was constructed by position coincidence of radio identifications in the Green Bank 1400 MHz sky maps (Condon & Broderick 1985, 1986; CB88) and galaxies in the *Uppsala General Catalogue of Galaxies* (Nilson 1973, hereafter referred to as UGC). Our sample consists of all galaxies in the CB88 sample which meet the following requirements: (1) Hubble type classification E or S0, (2) recession velocity < 7000 km s^{-1}, (3) optical major axis diameter $> 1'$ (this requirement follows from the UGC), (4) flux density > 150 mJy at 1400 MHz, (5) $-5^\circ < \delta < 82^\circ$, (6) having a 'monster' rather than a starburst energy source, as discerned from the IRAS/Radio flux ratio (CB88) and (7) a radio size $\geq 10''$ as measured from 1490 MHz VLA A array maps (see Xu et al. 1999a for a detailed description of the radio properties of the sample). The last requirement was chosen to ensure we only selected galaxies with radio jets. The resulting sample consists of 21 galaxies. Distances to the galaxies range between 15 Mpc and 90 Mpc. The sample covers a range of two magnitudes in absolute blue luminosity and a factor ~ 800 in radio-power (Fig. 1). The complete sample of galaxies is listed in Table 1, together with some general properties. All galaxies are classified as Fanaroff & Riley (1974) Type I (FR I) galaxies (Xu et al. 1999a).

2.2. The Data

We observed 14 galaxies with the `WFPC2` on board `HST` using the two broad-band filters `F555W` and `F814W` and 15 galaxies with a narrow-band filter centered on the Hα+[NII] emission lines. No HST data were taken for UGC 7115 and UGC 12064. For the remaining galaxies we used archival data with filters matching as closely as possible our program filters. The `F555W/F547M` and `F814W/F791W` filters correspond closely to the Johnson V- and Cousins I-band, respectively. Thus in total we have broad and narrow band observations for 19 of our 21 galaxies. Table 2 lists the observational setup for all exposures. The point spread function (hereafter PSF) of the `WFPC2` images has a typical FWHM $\sim 0.07''$. All observations were taken with the telescope guiding in fine lock, which typically gives an rms tracking-error of $0.003''$. A detailed description of the `WFPC2` instrument is given in the WFPC2 Instrument Handbook version 4.0 (Biretta et al. 1996).

2.3. Image Data Reduction

All images were calibrated with the standard `WFPC2` pipeline using the most up-to-date calibration observations [4]. This pipeline and other reduction tasks are available in the IRAF STSDAS package. We refer to the HST Data Handbook version 3.1 (ed. Voit 1998) for a detailed description of the calibration process.

For each broad-band filter two images were taken back to back to allow for cosmic-ray removal. For the narrow-band and LRF images, which have significantly longer exposure times, 3 or 4 images were taken back to back. We added the images and removed cosmic-rays with the 'crrej' task using an appropriate noise model for the `WPFC2`. Next we removed 'hot' pixels from the images using the 'warmpix' task. We then interpolated over remaining bad pixels using the 'wfixup' task. The final images are shown in Figure 6.

3. Isophotal Analysis

3.1. Reduction

We checked the alignment between the V and I band images using Galactic stars and/or globular clusters. If these objects could not be used we checked the alignment using the galaxy nucleus. Only a small sub-pixel shift was performed in one case (NGC 4261). All other images were aligned within 0.2 pixels (i.e. $0.01''$) and therefore no shifts for further alignment were performed.

We used the 'ellipse' task to perform isophotal fits to the light distributions of our targets. A detailed description of the method is given by Jedrzejewski (1987). We identified regions on the CCD which were not to be considered in the isophotal fitting procedure. These regions contain foreground stars, companion galaxies, globular clusters or regions affected by dust. The latter were identified by eye using the ratio of the V and I images in which local dust distributions clearly show up due to the differential opacity. However, this method is not sensitive to global smooth distributions of dust which might be present. A first fit was performed to the light distribution allowing center, position angle and ellipticity to vary freely for each radius. From these fits we determined the center of the luminosity distribution by taking the average of the center of ellipses within a certain radial range. A second fit was then performed but now with the center fixed during the fitting process. This procedure was performed separately on both the V- and I-band image for each galaxy. Additionally, the isophotal shape parameters determined for the I-band image were then used to determine the luminosity profile for the V-band image using these same parameters. We compared the resulting position angle (hereafter PA), ellipticity and Fourier coefficients from these different fitting procedures. Only insignificant differences were found which are likely due to low-level small dust features which could not be detected by inspecting the ratio

[4]No flatfields are available for the LRF filters. For these observations we used the nearest narrow-band flatfield available. This does not affect our results in any significant way.

image of V and I.

We derived a model for the galaxy from the isophotal fits, using the 'bmodel' task. We inspected the residuals between these model galaxies and the real galaxy image, and verified that the isophotal fits were indeed an accurate representation of the real galaxy. For several galaxies the dust distributions inhibited a free isophotal fit to the central regions. In these regions we fixed the isophotal parameters to the last isophotal fit performed just outside the dust region. Hence these inner surface brightness profiles are severely affected by dust obscuration. For the broad-band images it was not possible to determine the sky brightness from the `PC` images since the whole area of the `PC` chip and sometimes the `WF` chips as well were affected by light from the galaxies. We fitted a de Vaucouleurs profile to the region where the light contribution from the sky was negligible and extrapolated this profile to the regions on the `WF` chips affected by sky light. Thus the sky counts were defined as the difference between the observed counts and counts predicted from the extrapolation. The sky magnitudes have a narrow distribution around 22.5 mag arcsec^{-2} in V and 21.6 mag/arcsec^{-2} in I. The error in the sky counts is estimated to be 25%. We subtracted the sky counts from the surface brightness profile and determined V and I magnitudes using the 'synphot' task which yield typical errors in the absolute calibration of $\sim$ 0.05mag. Corrections were made for Galactic foreground extinction using optical extinction values A_V given by NED[5] which range between 0.0 and 0.44. The final luminosity profiles agree well with those inferred from ground-based data (see Appendix A). The derived isophotal parameters for the sample are shown in Figure 2.

3.2. Results

Luminosity Profiles

The luminosity profiles of galaxies with negligible or no dust affecting their isophotes clearly show a break radius at which the profile flattens off towards the center. What can we say about the luminosity profiles affected by dust obscuration? To get an indication we constructed 'un-extincted' luminosity profiles in Figure 2, using several assumptions. We assume that (i) the dust is distributed in a screen with a fixed fraction D of the total stellar light along the line of sight in front of it, (ii) the intrinsic color of the galaxy in the dust affected region is equal to the one just outside the dusty region (a plausible assumption based on the color profiles of galaxies without central dust) and (iii) a Galactic extinction law is valid. We can then use the color excess to derive the optical depth (see Appendix B) and hence the un-extincted surface brightness. Figure 3 shows the extinction in V magnitudes due to dust obscuration as function of observed color-excess for different screen positions. This figure illustrates that the observed color-excess provides a constraint on the un-extincted surface brightness only when D is known a priori. In reality, the distribution of the dust will certainly be more complex than that of a simple screen. To give nevertheless an indication of the possible corrections to the observed surface brightness

[5]The NASA/IPAC Extragalactic Database (NED) is operated by the Jet Propulsion Laboratory, California Institute of Technology, under contract with the National Aeronautics and Space Administration.

profiles we plotted in Figure 2 the un-extincted profiles assuming a front-screen (i.e., D=0; dashed line) and a 'mid-screen' (i.e., D=0.5; dotted lines). One of the mid-screen un-extincted profiles is almost identical to the front screen approximation (cf. Figure 3). Only color excess values in the range $[0, 0.2]$ can be observed for the mid-screen assumption (cf. Figure 3. The observed color excess in the central regions of the sample galaxies lies in most cases exactly within this range. This indicates that the screen approximations are at least consistent with the observed extinction. Our method is formally only correct if we observe a constant color-excess along each isophote. This is generally not true. However, simulations show that under the screen assumptions the method recovers the correct un-extincted isophotal magnitude to within 0.05^m for the typical observed color excess variations along isophotes. The un-extincted profiles show that the majority of the galaxies which do not show a break likely do have a break in their profile at some radius inside the dust affected region. But there are at least 2 galaxies (NGC 2329 and NGC 4335) for which a power-law all the way into the central region is probable assuming the central dust is located near the center of the galaxy. These two galaxies also have a high central surface brightness which is typical for galaxies with a steep central cusp. The absolute magnitudes in our sample scatter around the dividing range of magnitudes between 'cuspy' and 'shallow' cores (Faber et al. 1997). Hence it would be interesting to determine the distribution of central cusp slopes and break radii. This is not possible with our optical imaging due to the central dusty regions but requires high resolution near-infrared imaging. From the current data we can conclude that although obscuration by dust inhibits a direct determination of central cusp slopes, the data suggest most but not all galaxies have shallow cores.

Color Profiles
The $V-I$ color profiles (Fig. 2) provide limited information on the color of the stellar populations. In the inner regions most of our galaxies are severely affected by dust while in the outer regions the errors due to uncertain sky subtraction become large. The central color just outside the dust distributions in our sample range between 1.25 and 1.45. This agrees well with $V-I$ colors reported in other studies of giant ellipticals (Bender and Möllenhoff 1987; Carollo et al. 1997). Therefore we can only conclude that the sample galaxies have $V-I$ colors typical for giant ellipticals.

Position Angles
The variation of the position angle of the stellar isophotes over the measured range of radii is less than 10° for $\sim 50\%$ of the galaxies. The other half displays significantly larger isophotal twists. These could be due to low ellipticity and/or very shallow luminosity profiles. An additional possibility is the presence of small low-level dust obscuration which can not be detected from our V-I image and hence were missed during the masking (e.g., possibly in NGC 5127). Two galaxies, UGC 1841 and NGC 7626, show large twists which are undoubtly real (see also Sections A.6 and A.19). PA twists might be caused by either triaxiality or gravitational interaction.

Ellipticities
Using galaxy models we tested how the ellipticity of the inner isophotes is affected by the convolution with the PSF of `HST`. It turns out that this effect is negligible outside $r = 0.25''$ for our sample galaxies. In $\sim 35\%$ of the galaxies the ellipticity varies by 0.1 or more in the inner $10''$. Another $\sim 30\%$ show variations between 0.05 and 0.1. The remaining $\sim 35\%$ have variations less

than 0.05. We compared this with ellipticity variations in the inner 10″ of 41 radio-quiet, giant elliptical galaxies (i.e., $M_V \lesssim -19.5$), based on HST studies published by Lauer et al. (1995) and Carollo et al. (1997). For this sample of normal galaxies $\sim 45\%$, $\sim 40\%$ and $\sim 15\%$ show variations larger than 0.1, between 0.05 and 0.1 and less than 0.05, respectively. Thus radio-loud galaxies tend to have less variation in their ellipticity profiles in the inner 10″. However, this difference might be (partly) caused by the higher frequency of central dust in the inner few arcseconds in our radio-loud sample which could conceal variations.

Fourier Coefficients
The fourth order Fourier coefficient, c_4, describes the deviations of the isophotes from perfect ellipses. Negative values of c_4 indicate 'boxy' isophotes while positive values indicate 'disky' isophotes. In our sample departures from 0 are generally small (i.e. < 0.02) in the inner regions but sometimes persist over several arcseconds. There are two notable exceptions: UGC 1841 becomes very 'disky' around 10″ and NGC 4261 is very boxy outward of 2″. In our sample there are roughly equal numbers of galaxies with positive, negative c_4 and no departures. Bender et al. (1989) found that radio-loud galaxies tend to have 'boxy' isophotes at radii larger than several arcseconds. Interestingly, this is clearly not the case for the central few arcseconds of our radio-loud galaxies. The sample of Bender et al. includes all galaxies in our sample which are boxy but does not include most of the galaxies with elliptical or disky isophotes. We compared our central c_4 values with profiles beyond $\gtrsim 10''$ reported in previous studies (see Section A). In all but one of these the isophotal shapes are either similar or boxier at $r \gtrsim 10''$ than in the central region. The one exception is NGC 541.

4. Emission Gas Analysis

4.1. Reduction

To derive the flux from the Hα+[NII] emission lines we subtracted the contribution of stellar continuum light from the narrow band (i.e., the 'on-band') fluxes. We used the V- and I-band as 'off-band' images to estimate this continuum. Using these off-bands poses two potential problems. First, regions with gas emission are often affected by dust which has an opacity varying with wavelength. However, by estimating the continuum light distribution in the narrow-band images from a combination of the broad-band images on either side of the Hα frequency we are able to make a correction for the effects of dust as explained in more detail below. Second, the V-band filters include several emission lines (e.g., the far end of the `F555W` filter includes the Hα+[NII] emission lines). The I-band filters do not contain emission lines. We determined the contribution of emission-line flux to the stellar flux in the V band filters using our determined Hα+[NII] fluxes and assuming for each galaxy LINER emission-line ratios as found for M 87 by Dopita et al. (1997). The emission flux contributes at most 2.5% and is thus negligible. For NGC 4261 we used the `F675W` R-band image from the archive to measure the Hα+[NII] emission flux since no `HST` narrow-band observation is available. This passband includes also the [OI]$\lambda\lambda$6300, 6364 and [SII]$\lambda\lambda$6717, 6731 lines. For this galaxy, the latter lines contribute 50% of the emission-line flux in `F675W` (using again the M 87 line ratios). We did not make corrections for the slightly narrower

and broader PSF of the V and I filters, respectively, compared to the PSF of the narrow-band filter. We verified that by using the combination of V and I images as off-band image, these PSF differences alter the emission flux values by less than 5%.

First the broad-band images were aligned with the narrow-band image, using foreground stars and globular clusters or companion galaxies. In a few cases where these reference points were not available we assumed that the isophotal center of the narrow- and broad-band images coincide. For targets with narrow-band images on the `WF2` we rebinned the broad-band images on the `PC` to the larger `WF` pixel scale. From isophotal fits we determined the ratio between the on- and off-band fluxes in regions devoid of emission-line gas and dust. These ratios could be well fitted as a linear function of radius. Thus we could extrapolate this linear fit to regions with gas emission. We determined the observed emission flux $F_{\rm e}^{\rm obs}$ using the following equation:

$$F_{\rm e}^{\rm obs} = F_{NB}^{\rm obs} - \left(r_V \cdot F_V^{\rm obs} \cdot {\rm r}_I \cdot F_I^{\rm obs}\right)^{1/2}. \quad (1)$$

Here $F_j^{\rm obs}$ is the flux measured through filter j with NB denoting the narrow-band filter. The parameters r_V and r_I are the ratios of the continuum light in the narrow-band and the V- and I-band, respectively, and vary with radius. Next we explain that by using this combination of V and I as off-band we make a correction for the differential opacity at V, NB and I. To include the obscuration by dust we can write the more general version of eq. (1) as:

$$F_{\rm e}^{\rm obs} = F_{NB}^{\rm obs} - \left(r_V \cdot F_V^{\rm obs} \cdot {\rm r}_I \cdot F_I^{\rm obs}\right)^{1/2} \cdot \left(\frac{{\rm c}(NB) \cdot {\rm c}(NB)}{{\rm c}(V) \cdot {\rm c}(I)}\right)^{1/2}. \quad (2)$$

Here the correction factors $c(j)$ indicate the ratio between observed and intrinsic flux through filter j. If one assumes a 'front screen' of dust $c(j)$ becomes:

$${\rm c}(j) = e^{-\alpha_j \tau}, \quad (3)$$

where α_j is the opacity coefficient for filter j. If we define the 'total extinction factor' C as:

$${\rm C} = \left(\frac{{\rm c}(NB) \cdot {\rm c}(NB)}{{\rm c}(V) \cdot {\rm c}(I)}\right)^{1/2}, \quad (4)$$

and we take $\alpha_{\rm V} = 1.0$, $\alpha_{\rm NB} = 0.75$, $\alpha_{\rm I} = 0.5$ (consistent with a Galactic extinction law normalized to V), then C equals exactly 1 regardless of optical depth and eq. (2) reduces to eq. (1). Moreover, C remains within 2% percent of 1 for reasonable values of τ if one assumes the dust screen is placed in the middle of the galaxy (i.e., 50% of the stellar light originates in front and behind the screen) or if one assumes the dust is homogeneously mixed along the line of sight (see Fig. 4). For the latter two dust configurations the use of eq. (1) yields an under-estimate of the emission flux in areas affected by dust. The absolute flux calibration for the narrow-band filters for each galaxy was determined with the 'synphot' package which models the throughput for the `HST` filters and assuming all lines have zero width.

4.2. Results

The final Hα+[NII] emission images are shown in Figure 6. The derived fluxes are summarized in Table 3. Derived luminosities are typical for FR I galaxies (e.g., Zirbel & Baum 1995). All galaxies clearly show compact Hα+[NII] emission in their nucleus. In addition, some galaxies show extended low-surface-brightness emission features almost always associated with dust. Individual descriptions of the morphology of the emission gas can be found in Appendix A). Four remarks can be made concerning the final flux values. First, all emission fluxes are *observed* fluxes, i.e., are not corrected for extinction by dust. We did not attempt to correct for extinction because we can not reliably determine the distribution of dust relative to the emission gas. However, when we assume a front-screen of dust we can determine the amount of extinction using the observed $V-I$ color-excess per pixel in each galaxy (see Appendix B. It turns out that in this configuration the intrinsic flux can be typically at most 40% larger than the observed flux. Second, given the typical S/N of the emission images, we are only able to detect emission features with a surface brightness larger than $\sim 5 \cdot 10^{-15}$ ergs^{-1}cm^{-2}arcsec^{-2}. Thus extended low-surface-brightness features below this level will be undetected but might make up for a significant fraction of the total emission when integrated over the galaxy. Third, some galaxies reveal a nuclear point source that is bluer than the surrounding stellar light (see Section A. We did not adjust r_V and r_I for this. We verified that this results in an over-estimate of the total absolute flux up to $\sim 20\%$, assuming that the blue point source is caused by the contribution of a non-stellar continuum flux which results in the observed color. Fourth, the LRF, `F658`, `F673` filters have equivalent widths of $\sim$ 85Å, 28.5Å and 47.0Å, respectively and therefore a fraction of broad-line Hα+[NII] emission, if present, might fall outside the latter two passbands.

We compared the derived fluxes with values from the literature (see Table 3). The fluxes agree reasonably well except for two galaxies: NGC 741 and NGC 7626. For NGC 741 Macchetto et al. (1996) report an extended disk of emission. The average flux-density in this disk is well below our detection threshold. We could not find a reason for the discrepancy of NGC 7626.

5. DUST ANALYSIS

Dust is detected in 17 out of the 19 radio galaxies. This is consistent with the frequency of 72% ± 16% found by van Dokkum & Franx (1995) for another sample of radio galaxies imaged with `HST`.

Both galaxies without detected dust, NGC 741 and NGC 2892, are relatively far away. However, the minimal size of detected dust in our sample is 200 pc, which would still be resolved with `HST` (0.6″ and 0.45″ for NGC 741 and NGC 2892, respectively). It is possible that the location and/or optical depth of the dust feature produces too little reddening to be detected. Both galaxies are round ellipticals with large shallow cores (similar to M 87 which itself has little dust). They are also the only two galaxies in the sample with a very nearby apparent companion (angular separation $\leq 10''$). Both companions are featureless round ellipticals. These similarities suggest there may be similar reasons for not detecting the dust; either projection effects, or dust

destroying processes in the galaxy itself, or tidal interaction with the companion. In this respect it is also noteworthy that Macchetto et al. (1996) did report a disk of gas emission in NGC 741.

The dust properties are summarized in Table 4. There appear to be two distinct main classes of apparent (i.e., projected) dust morphologies: lanes and disks. To what extent is this distinction intrinsic or just due to different viewing angles? We found several differences which point in the direction of an intrinsic different morphology. The classification is robust: observed morphologies fall clearly in either classification bin. Only for NGC 5490 is the classification ambiguous but this is due to the very small size of the dust feature. The disks have a quite 'smooth' appearance. Their outlines closely resemble ellipses with sometimes spiral structures inside and small protuberances on the outside. Lanes have a quite irregular appearance. They show warps or bends and are often surrounded by secondary filaments and patches of dust. Dust disks tend to be closely aligned with the major axis of the stellar distribution while dust lanes do not display a clear preference of orientation (Fig. 5). In summary: there are various indications that the morphological difference between dust disks and lanes is intrinsic.

Physical sizes of the dust features range from 200 pc to 4.5 kpc. Dust features are typically smaller than ~ 1 kpc. The few features larger in size all show peculiar morphologies compared to the sub-kpc morphologies. This suggests that at least some of the larger dust features are still settling towards stable orbits. Physical sizes do not depend on the distance of the galaxy which suggests that our capability in detecting the dust features does not strongly depend on distance. There is also no indication of a correlation between size and morphology: both lanes and disks of similar sizes are present.

In general the minor axis of both lanes and disks appears to align roughly with the radio-jet axis (Fig. 5). A notable exception is NGC 7052 which has a misalignment of $\sim 40^\circ$. In NGC 3862 (3C 264) the optical jet interacts with the dust (Baum et al. 1998) which implies a large misalignment assuming the dust disk is physically thin. At the scales of 100 pc or larger, as detected here, the orientation of the dust lanes is influenced by the gravitational potential and by the pressure gradients of the hot gas. The relative importance of these forces, the destruction time scales, and dynamical evolution (i.e., settling of the dust in stable morphologies) are the factors determining the observed (mis)alignments (e.g., Quillen & Bower 1999). An analysis of the dust dynamics falls outside the scope of this paper and is deferred to a subsequent paper.

The dust masses were determined under the assumption that the dust is distributed in a screen at a given position with respect to the galaxy light. The dust mass $M_{\rm dust}$ is proportional to the optical extinction A_V (Sadler & Gerhard 1985; van Dokkum & Franx 1995):

$$M_{\rm dust} = \Sigma \cdot {\Gamma_V}^{-1} \cdot A_V = \Sigma \cdot {\Gamma_V}^{-1} \cdot -2.5 \log e^{-\alpha_V \tau}. \quad (5)$$

Here Σ is the area of the dust feature, Γ_V the visual mass absorption coefficient and α_V the extinction coefficient at V. The optical depth τ is determined as described in Appendix B. We adopt the Galactic value $\Gamma_V \sim 6 \times 10^6$ mag kpc$^2 M_\odot^{-1}$ since differences between the Galactic and elliptical galaxy extinction curves are generally small (Goudfrooij et al. 1994b). Table 4 lists the mass for two screen positions: in front of and halfway into the galactic light distribution. The dust mass increases typically by a factor of 3 by placing the screen halfway instead of in front

of the light distribution. There are two other main uncertainties affecting the mass estimates. First, the dust geometry is certainly more complex than a simple screen at one location in the galaxy. Second, there is no one-to-one connection between dust geometry and color excess (Witt et al. 1992; Witt & Gordon 1996 and see also Sec. 3.2). Therefore, the derived dust masses should be treated with caution and have mainly significance in a relative sense as a measure of the projected dust mass. Dust masses are usually smaller than a few times $10^4 M_{\odot}$. The more massive features show also the more extended peculiar morphologies, which are likely still settling down.

6. SUMMARY AND CONCLUSIONS

We have presented HST/WFPC2 broad- and narrow-band observations of 19 radio-loud early-type nearby galaxies which are part of a complete sample of 21 nearby Fanaroff & Riley Type I galaxies. We have described the data reduction, given isophotal fits and analysed the central emission-line gas and dust distributions. The general conclusion is that the centers of these FR I galaxies, apart from the ubiquitous presence of dust and gas distributions, resemble the centers of normal bright ellipticals. The galaxies have fairly round (ellipticity ≤ 0.3) stellar isophotes. Our radio-loud early-type galaxies seem to have on average less variation in their ellipticity profiles in the inner $10''$ compared to normal early-types of similar luminosity. However, this difference might be caused by the frequent obscuration by dust of the central regions of our sample galaxies. The shape of the isophotes is mostly close to perfect ellipsoidal ($|c_4| < 0.02$). Ground-based studies show that the isophotal shapes either remain similar or become boxier at radii beyond $10''$. The dust inhibits a direct measurement of the inner slope of the surface brightness profile. We applied simple models in which the dust is represented by a screen to estimate the possible range in slope for the un-extincted light profile in each galaxy. Most galaxies have profiles which do flatten off towards the nucleus. Two galaxies have light profiles which are consistent with a single power law slope. Thus at this stage both shallow and cuspy cores seem able to host an active nucleus which produces radio jets. Dust is detected in the cores of all but two sample galaxies. The dust morphology can be divided in three categories: disks, lanes and irregular distributions. Both disks and lanes have sizes ranging from a few hundreds of parsec to a few kiloparsec. The major axis of the disks is always aligned within a few degrees with the galaxy major axis while lanes have misalignments of tens of degrees and often show twists and warps. Therefore it is suggested that the difference between disks and lanes is intrinsic and not solely due to different viewing angles. The apparent major axis of both disks and lanes is generally roughly perpendicular to the radio jet axis. Two notable exceptions are NGC 7052 and NGC 3862. Using the narrow-band observations, we detected emission-line gas in the nucleus of each galaxy in our sample. Gas emission is also commonly associated with the dust distributions.

The dust and gas in the cores of these FR I galaxies provides a natural fuel supply for the active nucleus. The question which then can be raised is why the fraction of normal early-type galaxies which do show similar dust distributions in their cores do not host an AGN. Do these galaxies lack a massive BH to accrete the material and convert the gravitational energy? Or is the fuel, although clearly present, not funneled effectively to the nucleus due to differences in

the shape of the central gravitational potential well or differences in the ISM (e.g., pressure)? Thus it is important to perform a detailed comparitive study of these nearby active cores and normal quiescent cores. In this context we will obtain HST/STIS observations for the nuclei of the complete radio-loud sample to study the state and kinematics of the emission gas and constrain the mass of the BH.

Support for this work was provided by NASA through grant number #GO-06673.01-95A from the Space Telescope Science Institute, which is operated by AURA, Inc., under NASA contract NAS5-26555. TdZ gratefully acknowledges the warm hospitality of STScI. The authors would like to thank Roeland van der Marel and Marcella Carollo for helpful discussions and a critical reading of the manuscript, and the referee for helpful suggestions to improve the manuscript.

A. INDIVIDUAL PROPERTIES OF THE GALAXIES

In this appendix we give a separate description of each galaxy. We describe its environment, morphological features of the dust and emission gas apparent from our imaging and mention results from previous studies. We also compare our isophotal results to previous measurements. In most cases the results agree well. By this we mean that (at radii large enough for the isophotal parameters not to be affected by the point spread function of the observations) differences in surface brightness are less than 0.1^m, differences in ellipticity less than 0.02 and differences in PA less than 5°. We also briefly note the radio morphology on the arcsecond scale and larger. The radio properties of the sample will be described in more detail by Xu et al. (1999a) who made observations with the VLA and VLBA in snapshot mode. A study of the X-ray properties from `ROSAT` observations will be presented by Xu et al. (1999b).

A.1. NGC 193

NGC 193 is part of a group of galaxies (CB88) and has an apparent companion, NGC 204, at $6.7'$. NGC 193 shows a complex central dust distribution composed of patches and several warped filaments hundreds of parsec in size. The dust features are connected to each other. There is a nuclear emission peak which is marginally resolved. Low-surface-brightness emission is associated with the dust features. The center, although apparently obscured by dust, shows an unresolved peak clearly bluer than its surroundings. NGC 193 has a radio jet with a weak counter-jet (Xu et al. 1999a).

A.2. NGC 315

NGC 315 is part of Zwicky cluster 0107.5+3212 (Zwicky et al. 1961) which is located in the Perseus-Pisces filament. We detect a central dust disk 820 pc ($2.5''$) in diameter which is close to but not a perfect ellipse; the north tip of the disk has a small extension. In addition several mottled patches of dust are detected southwest of the nucleus out to $5''$ (~ 1.5 kpc). The central part of the dust disk forms a small bright emission-gas disk which extends into low-level emission throughout the dust disk. There is also a low-level emission feature adjacent to the southeast side (i.e., counter-jet side) of the dust disk which is elongated in the direction of the dust disk. HI was detected in absorption redshifted by ~ 400 km s^{-1} with respect to the systemic velocity (van Gorkom et al. 1989, Knapp et al. 1990). Ho et al. (1997) found a nuclear Hα broad-line emission component with FWHM 2000 km s^{-1} in addition to the narrow-line emission. Our isophotal analysis is in good agreement with an analysis by De Juan et al. (1994) from ground-based observations. The two-sided radio jet of NGC 315 has been well studied (e.g., Venturi et al. 1993; Bicknell 1994; Mack et al. 1997; Cotton et al. 1999).

A.3. NGC 383 (3C 31)

NGC 383 is the brightest galaxy in the Zwicky cluster 0107.5+3212 (Sakai et al. 1994). NGC 383 is inside a chain of galaxies and forms a dumbbell pair with Arp 331 (NGC 382) which is at 34″ (11 kpc). NGC 383 has a nearly face-on central dust disk (diameter 2.3 kpc/7.4″) which shows a spiral structure with a counter-clockwise orientation. The spiral structure becomes flocculent at the outer edges. Martel et al. (1999) detected a dust disk in the companion NGC 382 as well. NGC 383 has a central unresolved bright Hα+[NII] emission peak with low-surface-brightness emission extending out to $\sim 1''$ (300 pc) around it. Owen et al. (1990) detected a rotating extended emission disk from a spectroscopic study. NGC 383 has a nuclear point source clearly bluer than its surroundings. Komossa & Böhringer (1999) performed an X-ray study of the NGC 383 group and found indication for a hard X-ray component which might be associated with the central AGN. Our isophotal analysis is in very good agreement with previous ground-based studies by Fraix-Burnet et al. (1991) and De Juan et al. (1994). The latter found an increase in ellipticity from 0.1 to 0.3 outward of $r \sim 10''$. The radio jet has been extensively studied in the past (e.g., Lara et al. 1997 and references therein). The radio jet shows a distorted morphology suggesting gravitational interaction between NGC 383 and its companion NGC 382 (Blandford & Icke 1978; Parma et al. 1991). However, the optical isophotes out to scales larger than our HST imaging show no indication of interaction (Fraix-Burnet et al. 1991). Evidence for an optical jet was claimed by Butcher et al. (1980) but not confirmed by later studies (Keel 1988; Owen et al. 1990; Fraix-Burnet et al. 1991).

A.4. NGC 541

NGC 541 is located in Abell cluster 194 (Abell et al. 1989). It is located at 4.5′ (96 kpc) from the dumbbell pair NGC 545/NGC 547 identified with the radio source 3C 40 . NGC 541 has a central disk (diameter 640 pc/1.8″) which appears to be nearly face-on. The disk has an outer rim which is darker, especially on the north side. There is also an inner ring with radius $\sim 0.22''$ (78 pc) which shows enhanced obscuration. These darker ring-like structures could be part of an otherwise hardly visible spiral structure. The V-I image shows a hint of a linear dust feature with PA $\sim 267°$ sticking out of the disk. This is within 10° of the VLA radio jet axis (CB 1988). At the center of the dust disk there is a central Hα+[NII] emission peak. A ring of emission surrounds the peak just inside the darker rim of the disk. There is a slightly brighter emission spot at PA $\sim 51°$ and on the opposite side in the ring. The central pixels are slightly bluer than their surroundings. Our isophotal analysis agrees well with the study by De Juan et al. (1994). They find the abrupt increase in ellipticity outward of $\sim 10''$ to continue until 0.2 at 20″ and found a rise in the fourth order Fourier coefficient c_4 to 0.02 at $\sim 25''$. The radio-jets form a small head-tail source (O'Dea & Owen 1985) which might have triggered the starburst in Minkowski's object, an irregular dwarf, located in the path of the jet at 45″ (16 kpc) NE of NGC 541 (van Breugel et al. 1985).

A.5. NGC 741

NGC 741 is the brightest galaxy in a group of galaxies (Zabludoff & Mulchaey 1998). There is a small apparent elliptical companion at $\sim 8''$ (2.7 kpc assuming same distance) which is not cataloged in NED. A second elliptical companion, NGC 742, is located at $48''$ (16.2 kpc). No dust is detected in NGC 741. We detect a central peak of emission with low level emission filaments extending $\sim 2''$ (680 pc) towards the North, East and South. Macchetto et al. (1996) detected an emission-gas disk from the ground with minor and major diameter of $10.8''$ (3.7 kpc) and $22.6''$ (7.7 kpc) respectively, and with an average flux density which is significantly below our detection threshold. This disk fills most of the PC. NGC 741 hosts a head-tail radio source (Birkinshaw & Davies 1985).

A.6. UGC 1841 (3C 66B)

UGC 1841 forms a dumbbell pair with a companion southeast at a distance of $\sim 24''$ (10 kpc). The pair belongs to a small group of galaxies close to the Abell cluster 347. UGC 1841 has a central dust disk (diameter 330 pc/$0.8''$) which appears to be neither a perfect ellipse nor a circle. There is a protuberance $\sim 0.25''$ (~ 100 pc) in length with PA 230°. The emission image shows bright nuclear Hα+[NII] emission slightly extended towards PA 228°. Intriguingly, both the slight extension of the Hα+[NII] emission and dust protuberance of the disk are in the direction of the counter jet (Fraix-Burnet 1997). The optical jet was detected by Butcher et al. (1980) and studied by Keel (1988) and Fraix-Burnet et al. (1989, 1991). The surface brightness of the optical jet is quite low and therefore hardly detectable on our images but clearly shows up once a model galaxy is subtracted. A tentative optical counter-jet is reported by Fraix-Brunet (1997) from a 15 hour I-band exposure. Our isophotal analysis agrees well with Fraix-Burnet et al. (1991). They found the same PA twist. We excluded the region affected by the bright star on the PC from the fit. We also confirm the reported offset toward PA 70° of the isophotal centers increasing to $3''$ at $r \sim 20''$. The radio jet displays a distorted double-sided jet structure (Hardcastle et al. 1996).

A.7. NGC 2329

NGC 2329 is part of Abell cluster 569. The galaxy has a small inclined central dust disk (diameter 740 pc/$2.0''$). The V-I image shows a few brighter pixels over the disk ending in a lighter spot at the edge of disk at PA 318°. There also seems to be a small dust protuberance to the disk in the opposite direction. The nuclear emission is slightly resolved and shows a small extension roughly in the direction of the dust protuberance. The nucleus is clearly bluer than its surroundings. The galaxy has an exceptional blue V-I (~ 1.20) color compared to the rest of the sample. NGC 2329 hosts a wide-angle tailed radio source (Feretti et al. 1985; Xu et al. 1999a).

A.8. NGC 2892

NGC 2892 is an isolated galaxy apart from a nearby apparent elliptical companion at $\sim 10''$ (4.4 kpc assuming same distance) which is not identified in NED. No dust is detected in NGC 2892. The emission image shows a central peak with low-level emission around it out to $\sim 0.3''$ (130 pc). The V-I image shows a blue nuclear point source. NGC 2892 has a very regular double-sided radio jet (CB88; Xu et al. 1999a).

A.9. NGC 3801

NGC 3801 is inside a group of ten galaxies (Garcia 1993). It has a very extended and complicated dust distribution. There is a main dust lane ($\sim$ 4.4 kpc/$21''$) perpendicular to the major axis of the galaxy with a warped and stranded structure. A second filamentary dust distribution extends roughly perpendicular to the east-side of the main dust lane while on the west side there are about six thinner parallel filaments also roughly perpendicular to the main dust lane. This structure spans $\sim 60''$ (12.6 kpc) and is visible on both the PC and WF. Hα+[NII] emission is detected $\sim 0.5''$ ($\sim$ 100 pc) away from the dust enshrouded nucleus itself. There are about a dozen 'knots' of emission along the main dust lane. The 'knots' appear to be connected by 'bridges' of low level emission. Some of the knots are slightly resolved. The brightest 'knots' coincide with slightly brighter small spots in the V-band image and are likely to be star forming regions. HI is detected in emission (Heckman et al. 1983) and also in absorption with an estimated mass of $2.1 \cdot 10^9$ $M_\odot$ (Duprie et al. 1996). Radio maps by Jenkins (1982) and Xu et al. (1999a) show a warped double-lobed profile roughly perpendicular to the main dust lane. Our isophotal analysis agrees with R-band photometry by Peletier et al. (1990). There is an estimated $\sim 0.5''$ uncertainty in the determined center of the isophotes due to the very large extent of the dust distribution which affects a large fraction of the PC image. Ground-based images (Heckman et al. 1986) show that the galaxy becomes quite boxy at $r \sim 30''$.

A.10. NGC 3862 (3C 264)

NGC 3862 is part of the cluster Abell 1367 and has a nearby lenticular companion (IC 2955) at a distance of $54''$ (22 kpc). There is an apparent faint face-on circular dust disk (Crane et al. 1993) 610 pc ($1.5''$) in diameter which is studied in detail by Baum et al. (1997). The apparent disk is edge-darkened, especially the southern half. This might be a projection effect or could indicate that the inner parts of the dust disk are swept clear by either the jet or some other nuclear process (Hutchings et al. 1998). The Hα+[NII] emission is strongly peaked at the nucleus and diffuse low-level emission is seen throughout the disk. There is a strong blue nuclear point source. 3C 264 is a head-tail radio source displaying S-shaped wiggles extending to a long bifurcated tail of diffuse radio emission (e.g., Baum et al. 1988; Parma et al. 1991; Lara et al. 1999). The optical jet, discovered by Crane et al. (1993), seems to interact with the surrounding ISM (Baum et al. 1997).

A.11. NGC 4261 (3C 270)

NGC 4261 is the main galaxy in a group of 33 galaxies (Nolthenius 1993) in the 'Virgo West' cloud. It is a prolate galaxy with stellar rotation around the apparent major axis (Davies & Birkenshaw 1986). NGC 4261 has a small nuclear dust disk (diameter 240 pc/1.7″) discovered by Jaffe et al. (1993). Darker and lighter streaks are present in the disk suggesting a spiral structure. The V-band image shows a clear jet-like dust protuberance $\sim 0.65''$ (~ 90 pc) in length sticking out of the disk and pointing from the nucleus. There is a weaker similar dust feature on the opposite side. Both features were already noted by Ferrarese et al. (1996). They also noted a small (~ 5 pc/0.035″) offset between the center of the dust disk and the nucleus on the one hand and center from the isophotes on the other. By modeling the central gas kinematics they detect a black hole with mass $\sim 5 \cdot 10^8$ $M_\odot$. Möllenhoff & Bender (1987) detected in addition to the central dust disk a dust feature at $\sim 15''$ (2.1 kpc) north of the nucleus which falls outside our image. Jaffe & McNamara (1994) detected central HI and CO in absorption. The dust obscured nucleus shows a faint blue point source. NGC 4261 has a double-sided radio-jet (e.g., Birkenshaw & Davies (1985); Jones & Wehrle 1997). Our isophotal analysis agrees well with the analysis by Ferrarese et al. (1996) who use the same `HST` observations and with an analysis from ground-based data (Peletier et al. 1990). The latter shows a very constant PA out to $\sim 100''$ while the ellipticity decreases to ~ 0.15 and the Fourier coefficient c_4 becomes 0.

A.12. NGC 4335

NGC 4335 is a field galaxy without nearby companions. Arc shaped dust features (with a total diameter of 4 kpc/13.5″) surround the nucleus and appear to be the visible half of a settling dust disk. The outer parts consist of 'arms' of dust while the inner parts are formed by a small central dust disk (diameter ~ 240 pc/0.8″) embedded in a larger dust disk (diameter ~ 750 pc/2.5″) with similar axial ratio and PA. There is nuclear Hα+[NII] emission and low-level emission is associated with the extended dust features throughout the galaxy. Knapp & Rupen (1996) report a tentative detection of CO in absorption. NGC 4335 hosts a two-sided radio jet (CB88; Xu et al. 1999a).

A.13. NGC 4374 (M 84, 3C 272.1)

NGC 4374 resides in the Virgo cluster and is part of Markarian's Chain. The two filamentary dust lanes (total size ~ 1 kpc/13.0″) which flare at the ends have been known for a long time (e.g., Hansen et al. 1985; van Dokkum & Franx 1995; Bower et al. 1997). The PA of the dust lane and the stellar distribution differ by $50 - 60°$. Quillen & Bower (1999) recently proposed a model in which the misalignment and the warps of the dust lanes are caused by jet-induced pressure gradients. Our emission image agrees well with results found by Bower et al. (1997) using a different subtraction technique. NGC 4374 has a central emission-gas disk and lower level emission which follows the dust distribution. Bower et al. (1998) derived a black hole mass of

$\sim 1.5 \cdot 10^9$ $M_\odot$ from velocities measured in the central emission-gas disk. Deeper imaging of the emission gas shows an 'S'-shaped twist from PA $\sim 70°$ to $\sim 115°$ at $r \sim 7''$ (Hansen et al. 1985; Baum et al. 1988). Although the nucleus is most likely obscured by dust it is clearly bluer than its surroundings. M 84 has a two-sided radio jet (Jones et al. 1981; Laing and Bridle 1987).

A.14. NGC 4486 (M 87, 3C 274)

M 87 is the second brightest galaxy in Virgo. The dust in M 87 is made up of irregular patches and filaments which can be seen out to $\sim 11''$ (820 pc) from the nucleus. The central emission gas was first studied with HST by Ford et al. (1994) and Harms et al. (1994). An isophotal fit to our central emission features agrees very well with their results. Studies of the emission-gas kinematics yield a black hole with a mass of $\sim 3.2 \cdot 10^9$ $M_\odot$ (Harms et al. 1994; Macchetto et al. 1997). Irregular spiral arms of emission extend from the disk and emission gas is associated with all dust features. Dopita et al. (1997) showed that the off-nucleus emission-gas has a LINER spectrum and is excited by shocks. Carter et al. (1997) found evidence for many small dense clouds of gas in the core of M 87 with a velocity range ~ 300 kms using high resolution ground-based spectroscopy. The active nucleus in M 87 emits a non-stellar continuum which is reported to vary in strength over time in the optical (Tsvetanov et al. 1998) and X-rays (Harris et al. 1997). The optical and radio jet have been studied extensively (e.g., Meisenheimer et al. 1996 for a recent review; Biretta 1998; Perlman 1999). M 87 has an apparent one-sided optical and radio jet but there are strong indications for a counter-jet (Sparks et al. 1992; Stiavelli et al. 1992, 1997). Our isophotal analysis is consistent with studies by Ferrarese et al. (1994) and Peletier et al. (1990). The latter find that the ellipticity increases monotonically to 0.15 between $10''$ and $\sim 100''$. This increase enables a more robust estimate of the PA for this region which decreases from $\sim 170°$ to $145°$.

A.15. NGC 5127

NGC 5127 is the second brightest galaxy in Zwicky cluster 1319.6+3135. It has a bended dust lane (size 940 pc/$3.0''$) across the center which forks in two towards the northeast. There is a compact nuclear emission peak surrounded by low-surface-brightness emission associated with the dust lanes. NGC 5127 has a symmetric two-sided VLA radio jet (Xu et al. 1999a). Our isophotal analysis agrees well with an analysis by De Juan et al. (1994). They report the same PA twist and find that the isophotes become increasingly boxy beyond $r \sim 10''$.

A.16. NGC 5141

NGC 5141 is part of a group of six galaxies (Ramella et al. 1989) and has a companion galaxy, NGC 5142, at $2.3'$ (47 kpc). It has a central slightly wedge-shaped dust lane with a size of 800 pc ($2.3''$). The Hα+[NII] emission peaks at the center and low-level emission is detected in the dust lane. NGC 5141 has two-sided radio jets with broad lobes (Xu et al. 1999a). Our

isophotal analysis is consistent with a ground-based study by González-Serrano et al. (1993). In contrast with our results, however, they report a sharper decrease in ellipticity inward of 3″. This difference might be caused by their larger seeing and/or a distortion of the inner isophotes by the central dust distribution.

A.17. NGC 5490

NGC 5490 is the brightest galaxy in Zwicky cluster 1407.6+1750. There is a very small central dust distribution 0.5″ (170 pc) in size with PA 143°. It appears to be either a dust lane or a highly inclined disk. There is a compact central peak of Hα+[NII] emission. NGC 5490 hosts a double-sided radio jet (CB88; Xu et al. 1999a). Our isophotal analysis agrees with a study by De Juan et al. (1994). They found a lower ellipticity in the inner few arcseconds, but poor seeing is the most likely cause for this. They also note a 15° increase of PA outward of 10″.

A.18. NGC 7052

NGC 7052 is a field galaxy with no nearby companion. There is a large central dust disk with a diameter of 1 kpc (4.0″) (De Juan et al. 1996). The inner part of the dust disk hosts a small emission-gas disk and low-level emission is detected throughout the dust disk. By modeling the kinematics of the gas disk van der Marel & van den Bosch (1998) detected a black hole with a mass of $\sim 3 \cdot 10^8$ $M_\odot$. There is a dust protuberance, also seen in the emission image at the west end of the disk. HI was detected in emission blueshifted by $\sim$ 500km s^{-1} with respect to the systemic velocity of the galaxy (Huchtmeier et al. 1995). The nucleus which is obscured by dust is slightly bluer than its surroundings. NGC 7052 hosts a narrow radio jet with a very weak counter jet (Morganti et al. 1987; CB88; Xu et al. 1999a). Our isophotal analysis agrees well with previous studies (De Juan et al. (1994); van den Bosch & van der Marel 1995; van der Marel & van den Bosch 1998). De Juan et al. found the ellipticity to increase until $\sim$ 0.55 at $\sim$ 30″ and the isophotes to become boxy outward of 10″.

A.19. NGC 7626

NGC 7626 has a nearby higher luminosity companion NGC 7619 which is at 6.8′ (90 kpc). They are the two brightest ellipticals in the Pegasus I cluster. NGC 7626 has a counter rotating core (Forbes et al. 1995; Carollo et al. 1997). There is a small warped dust lane (diameter 230 pc/1.0″) across the nucleus. Interestingly the central part of the dust lane is perpendicular to the radio jet while the warped outer part aligns with the major axis of the galaxy. There is an unresolved nuclear emission peak and low-level emission gas is seen along the dust lane. NGC 7626 has double-sided radio lobes (Xu et al. 1999a). Our isophotal analysis is in good agreement with previous ground-based (Peletier et al. 1990; De Juan et al. 1994) and HST studies (Carollo et al. 1997). The PA of the isophotes increases by 20° in the central 10″. Forbes & Thomson (1992)

reported excess light in the galaxy which might be due to tidal interaction with NGC 7619.

B. Optical depth

Following Carollo et al. (1997), we derive the optical depth under the assumption that the dust distribution can be represented by a screen. For a dust screen at position D relative to the distribution of light along the line of sight ($D = 0$ for a screen in front of the galaxy and $D = 1$ behind the galaxy) we can write the ratio between intrinsic and observed fluxes as:

$$r_j = \frac{F_j^{\rm obs}}{F_j^{\rm int}} = D + (1 - D)e^{-\alpha_j \tau}, \tag{B1}$$

where r_j is the ratio of $F_j^{\rm obs}$ and $F_j^{\rm int}$, i.e. of the observed and intrinsic flux through filter j ($j = V, I$), respectively. The extent and morphology of the dust distributions inhibit a direct estimate of these two ratios from our isophotal analysis to derive τ. However, the ratio $r_{VI}^{\rm int}$ of the un-extincted flux in V and in I (i.e., its color) is well fitted as a slowly varying linear function of radius for the centers of these early-type galaxies. This fit can be extrapolated into regions affected by dust. Thus we determine from our imaging the ratio a_{VI} between the un-extincted and observed color which can be written as:

$$a_{VI} \equiv \frac{r_{VI}^{\rm obs}}{r_{VI}^{\rm int}} \equiv \frac{r_V}{r_I} = \frac{D + (1 - D)e^{-\alpha_V \tau}}{D + (1 - D)e^{-\alpha_I \tau}}. \tag{B2}$$

Taking $\alpha_V = 1.0$ and $\alpha_I = 0.5$ (consistent with Galactic extinction) and substituting $t = e^{-0.5\tau}$, eq. (B2) becomes a second order equation which can be solved analytically for τ.

REFERENCES

Abell G.O., Corwin H.G., Olowin R.P., 1989, ApJS, 70, 1

Baum S.A., Heckman T.M., Bridle A., van Breugel W., Miley G., 1988, ApJS, 68, 643

Baum S.A., et al. , 1997, ApJ, 483, 178

Bender R., Möllenhoff C., 1987, A&A, 177, 71

Bender R., Surma P., Döbereiner S., Möllenhoff C., Madejsky R., 1989, A&A, 217, 35

Bicknell G.V., 1994, ApJ, 422, 542

Biretta J., et al. , 1996, Wide Field and Planetary Camera 2 Instrument Handbook, Version 4.0, STScI, Baltimore

Biretta J.A., Perlman E., Sparks W.B., Macchetto F., 1998, HST preprint no. 1271, to be published in proceedings of the M 87 Workshop at Ringberg Castle, 1997

Birkenshaw M., Davies R.L., 1985, ApJ, 291, 32

Blandford R.D., Icke V., 1978, MNRAS, 185, 527

Bower G.A., Heckman T.M., Wilson A.S., & Richstone D.O., 1997, ApJ, 483, L33

Bower G.A., et al. , 1998, ApJL, 492, L111

Butcher H.R., van Breugel W., Miley G.K., 1980, ApJ, 235, 749

Carollo C.M., Franx M., Illingworth G.., Forbes D.A., 1997, ApJ, 481, 710

Carter D., Johnstone R.M., Fabian A.C., 1997, MNRAS Letters, 285, L20

Condon J.J., Broderick J.J., 1985, AJ, 90, 2540

Condon J.J., Broderick J.J., 1986, AJ, 96, 1051

Condon J.J., Broderick J.J., 1988, AJ, 96, 30 (CB88)

Cordey R.A., 1986, MNRAS, 219, 575

Cotton W.D., Feretti L., Giovannini G., Lara L., Venturi T., 1999, ApJ in press (astro-ph[9902053])

Crane P., et al. , 1993, ApJL, 402, L37

Davies R.L., Birkenshaw M., 1986, ApJL, 303, L45

De Juan L., Colina L., Pérez-Fouron, 1994, ApJ Suppl., 91, 507

De Juan L., Colina L., & Golombek D., 1996 A&A, 305, 776

de Koff S., et al. , 1999, submitted to ApJ

Disney M.J., Sparks W.B., Wall J.V., 1984 MNRAS, 206, 899

Dopita M.A., et al. , 1997, ApJ, 490, 202

Duprie K., Schneider S.E., 1996, AJ, 112, 937

Faber S.M., et al. , 1989, ApJS, 69, 763

Faber S.M., et al. , 1997, AJ, 114, 1771

Fanaroff B.L., Riley F.M., 1974, MNRAS, 167, 31

Feretti L., Giovannini G., Gregorini L., Padrielli L., Roland J., Valentijn E.A., 1985, A&A, 147, 321

Ferrarese L., van den Bosch F.C., Ford H.C., Jaffe W., O'Connell R.W., 1994, AJ, 108, 1598

Ferrarese L., Ford H.C., Jaffe W., 1996, ApJ, 470, 444

Forbes D.A., Thomson R.C., 1992, MNRAS, 254, 723

Forbes D.A., Franx M., Illingworth G.D., 1995, AJ, 109, 1988

Ford H.C., et al. , 1994, ApJL, 435, L27

Ford H.C., Tsvetanov Z.I., Ferrarese L., & Jaffe W., 1998, in Proceedings IAU Symposium 184 (Dordrecht: Kluwer Academic Publishers), in press [astro-ph/9711299]

Fraix-Burnet D., Nieto J.-L., Leliévre G., Macchetto F.D., Perryman M.A.C., di Serego Alighieri S., 1989, ApJ, 336, 121

Fraix-Burnet D., Golombek D., Macchetto F.D., 1991, AJ, 102, 562

Fraix-Burnet D., 1997, MNRAS, 284, 911

Garcia A.M., A&A Suppl., 1993, 100, 47

González-Serrano J.I., Carballo R., Pérez-Fournon I., 1993, AJ, 105 1710

Goudfrooij P., Hansen L., Jorgensen H.E., Nørgaard-Nielsen H.U., 1994a, A&A Suppl., 105, 341

Goudfrooij P., de Jong T., Hansen L., & Nørgaard-Nielsen H.U, 1994b, MNRAS, 271, 833

Hansen L., Nørgaard-Nielsen H.U., Jørgensen H.E., 1985, A&A, 149, 442

Hardcastle M.J., Alexander P., Pooley G.G., Riley J.M., 1996, MNRAS, 278, 273

Harms R.J., et al. , 1994, ApJL, 435, 35

Harris D.E., Biretta J.A., Junor W., 1997, MNRAS, 284, 21

Heckman T.M., Balick B., van Breugel W.J.M., Miley G.K., 1983, AJ, 88, 583

Heckman T.M. et al. , 1986, ApJ, 311, 526

Ho L.C., Filippenko A.V., Sargent W.L.W., Peng C.Y., 1997, ApJS, 112, 391

Ho L., 1998, in Observational Evidence for Black Holes in the Universe, ed. S.K. Chakrabarti (Dordrecht: Kluwer Academic Publishers), in press [astro-ph/9803307]

Huchtmeier W.K., Sage L.J., Henkel C., 1995, A&A, 300, 675

Hummel E., Kotanyi C.G., 1982, A&A, 106,183

Hummel E., Kotanyi C.G., Ekers R.D., 1983 A&A, 127, 205

Hutchings J.B., Baum S.A., Weistrop D., Nelson C., Kaiser M.E., Gelderman R.F., 1998, AJ, 116, 634

Jaffe W., Ford H.C., Ferrarese L., van den Bosch F.C., O'Connell R.W., 1993, Nature, 364, 213

Jaffe W., Ford H.C., O'Connell R.W., van den Bosch F.C., Ferrarese L., 1994, AJ, 108, 1567

Jaffe W., McNamara B.R., 1994, ApJ, 434, 110

Jedrzejewski R.I., 1987, MNRAS, 226, 747

Jenkins C.R., 1982, MNRAS, 200, 705

Jones D.L., Sramek R.A., Terzian Y., 1981 ApJ, 246, 28

Jones D.L., Wehrle A.E., 1997, ApJ, 484, 186

Keel W.C., 1988, ApJ, 329, 532

Knapp G.R., Bies W.E., van Gorkom J.H., 1990, AJ, 99, 476

Knapp G.R., Rupen M.P., 1996, ApJ, 460, 271

Komossa S., Böhringer, 1999, A&A, in press

Kormendy J., Stauffer J., 1987, Proceedings IAU Symposium 127, Kluwer Academic Publishers, ed. P.T. de Zeeuw, p. 405

Kormendy J., Richstone D., 1995, ARA&A, 33, 581

Kotanyi C.G., Ekers R.D., 1979, A&A Letters, 73, L1

Laing R.A., Bridle A.H., 1987, MNRAS, 228, 557

Lara L., Cotton W.D., Feretti L., Giovannini, Venturi T., Marcaide J.M., 1997, ApJ, 474, 179

Lara L., et al. , 1999, ApJ, in press, [astro-ph/9810495]

Lauer T.R., et al. , 1995, AJ, 110, 2622

Lynden-Bell D., 1996, MNRAS, 279, 389

Macchetto F., et al. , 1996, A&A Suppl., 120, 463

Macchetto F., Marconi A., Axon D.J., Capetti A., Sparks W., Crane P., 1997, ApJ, 489, 579

Mack K.-H., Klein U., O'Dea C.P., Willis A.G., A&A Suppl., 1997, 123, 423

Martel A.R., et al. , 1998, ApJ, 496, 203

Martel A.R., et al. , 1999, ApJS, 122, in press

Meisenheimer K., Röser H.-J., Schlötelberg M., 1996, A&A, 307, 61

Möllenhoff C., Bender R., 1987, A&A, 174, 63

Morganti R., Fanti C., Fanti R., Parma P., de Ruiter H.R., 1987, A&A, 183, 203

Morganti R., Ulrich M.-H., Tadhunter C.N., 1992, MNRAS, 254, 546

Nilson P., 1973, *Uppsala General Catalogue of Galaxies* (Uppsala Astronomical Observatory, Uppsala

Nolthenius R., 1993, ApJS, 85, 1

O'Dea C.P., Owen F.N., 1985, AJ, 90, 954

Owen F.N., Laing R.A., 1989, MNRAS, 238, 357

Owen F.N., O'Dea C.P., Keel W.C., 1990, ApJ, 352, 44

Parma P., Cameron R.A., de Ruiter H.R., 1991, AJ, 102, 1960

Peletier R.F., Davies R.L., Illingworth G.D., Davis L.E., Cawson M., 1990, AJ, 100, 1091

Perlman E.S., Biretta J.A., Zhou F., Sparks W.B., Macchetto F.D., 1999, AJ, in press

Quillen A.C., Bower G.A., 1999, submitted to ApJ, [astro-ph/9812312]

Ramella M., Geller M. J., Huchra J.P., 1989, ApJ, 344, 57

Rees M., 1984, ARA&A, 22, 471

Richstone D., 1998, in Proceedings IAU Symposium 184 (Dordrecht: Kluwer Academic Publishers), in press

Sadler E.M., & Gerhard O.E., 1985, MNRAS, 214, 177

Sadler E.M., 1997, The Nature of Elliptical Galaxies, ASP Conference Series, vol. 115, p. 411, eds. Arnaboldi, M., Da Costa, G.S. and Saha, P.

Sakai S., Giovanelli R., Wegner G., 1994, AJ, 108, 33

Sparks W.B., Fraix-Burnet D., Macchetto F., Owen F.N., 1992, Nature, 355, 804

Sparks W.B., Biretta J.A., Macchetto F., 1994, ApJS, 90, 909

Stiavelli M., Biretta J., Möller P., Zeilinger W.W., 1992, Nature 355, 802

Stiavelli M., Peletier R.F., Carollo C.M., 1997, MNRAS, 285, 161

Tsvetanov Z.I., et al. , 1998, ApJL, 493, L83

van Breugel W., Filippenko A.V., Heckman T.M., Miley G., 1985, ApJ 88, 40

van den Bosch F.C., van der Marel R.P., 1995, MNRAS, 274, 884

van der Marel, R. P. 1998, Proceedings IAU Symposium 186, Kluwer Academic Publishers, eds. Sanders, D. B., Barnes, J., in press

van der Marel R.P., van den Bosch, F.C., 1998, AJ, 116, 2220

van Dokkum P.G., Franx M., 1995, AJ, 110, 2027

van Gorkom J.H., et al. , 1989, AJ, 97, 708

Venturi T., Giovannini G., Feretti L., Comoretto G., Wehrle A. E., 1993, ApJ, 408, 81

Voit M. (ed.), et al. , 1997, HST Data Handbook, Volume I, Update Version 3.1 March 1998, STScI, Baltimore

Wagner S.J., Witzel A., 1995, ARA&A, 33, 163

Witt A.N., Thronson H.A., Capuano J.M., 1992, ApJ, 393, 611

Witt A.N., Gordon K.D., 1996, ApJ, 463, 681

Xu C., et al. , 1999a, in preparation

Xu C., et al. , 1999b, in preparation

Zabludoff A.I., Mulchaey J.S., 1998, ApJ, 496, 39

Zirbel E.L., Baum S.A., 1995, ApJ, 448, 521

Zwicky F., Herzog E., Wild P., Karpowicz M., Kowal C.T., 1961-1968, Catalogue of Galaxies and Cluster of Galaxies, Pasadena: California Institute of Technology

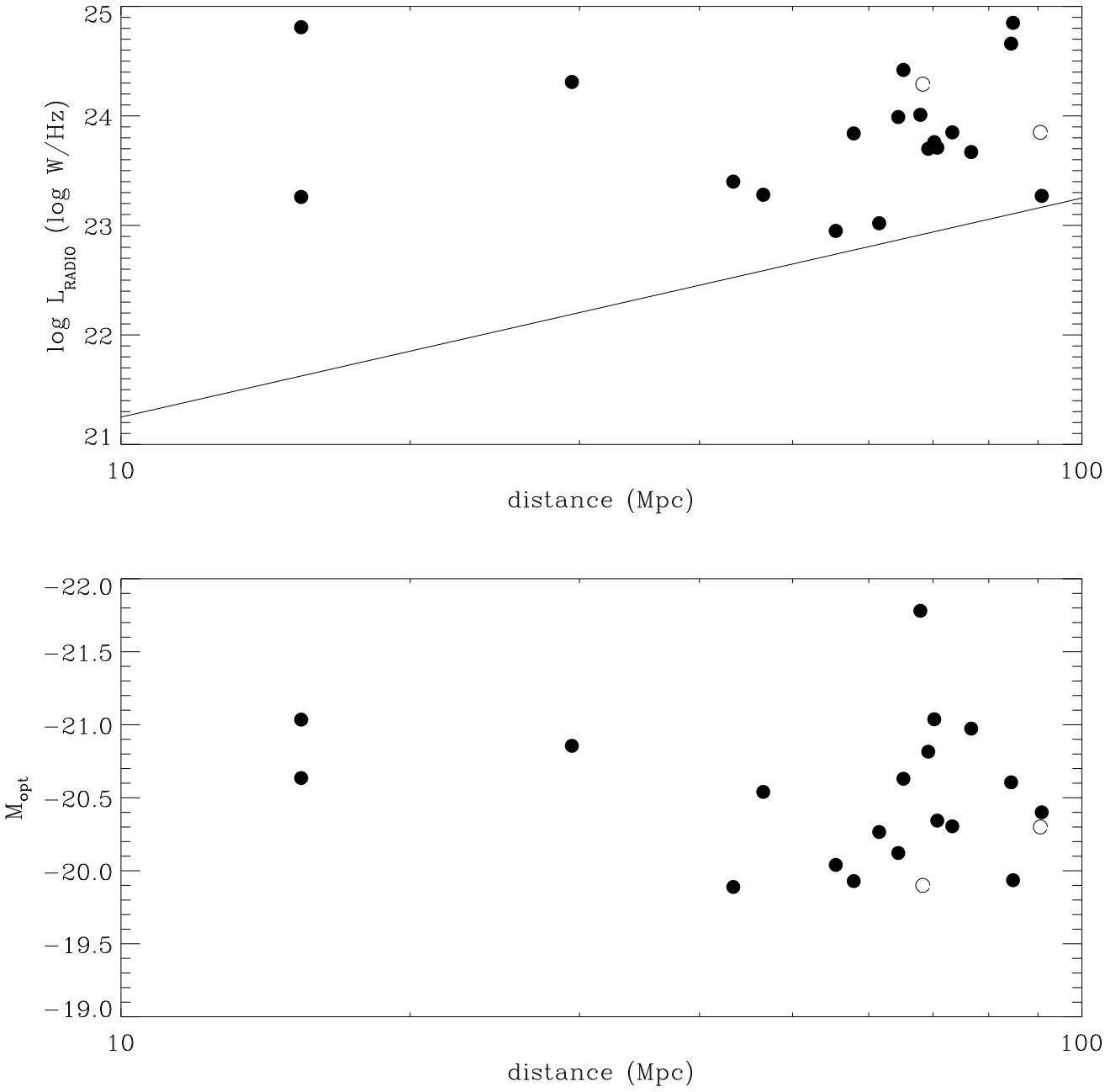

Fig. 1.— Total luminosities as a function of distance for the complete sample. The 19 galaxies presented in this paper are shown as filled dots. Top: total radio luminosity at 1400 MHz. The solid line indicates the lower cut-off of the radio luminosity set by our selection. Bottom: absolute photographic magnitude.

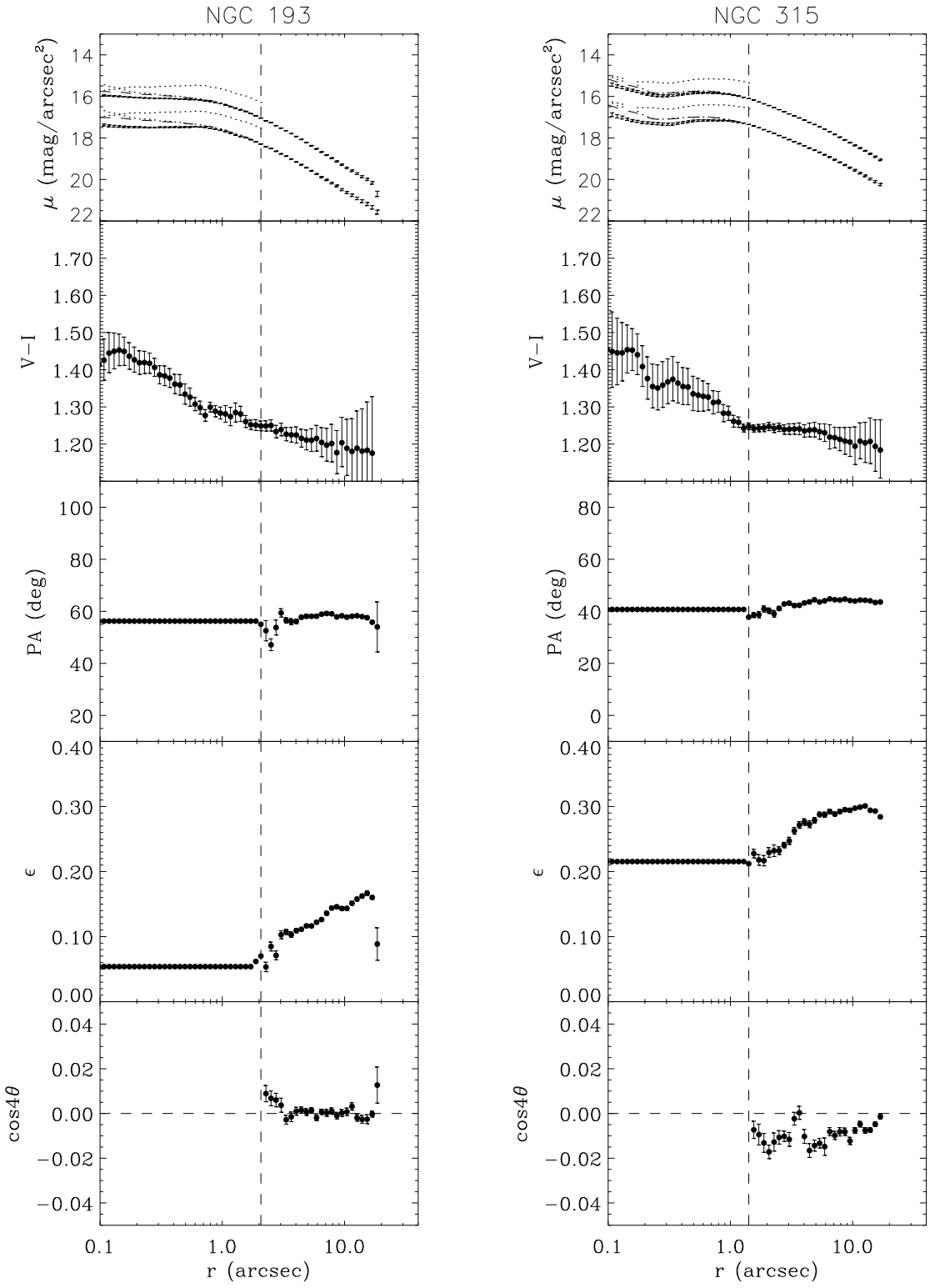

Fig. 2.— Isophotal parameters in the I-band as function of radius along the major axis. From top to bottom: surface brightness, V-I color, position angle, ellipticity and fourth order Fourier coefficient. The galaxy name is shown above each column. The top plot also shows the V-band luminosity profile (i.e. higher μ). The dashed and dotted lines display luminosity profiles corrected for dust obscuration (see Section 3). Error bars include the formal error given by the isophotal fitting routine and the error in the estimated sky counts. The vertical dashed line indicates the maximum radius out to which the isophotes are affected by dust obscuration and PA and ϵ are kept fixed.

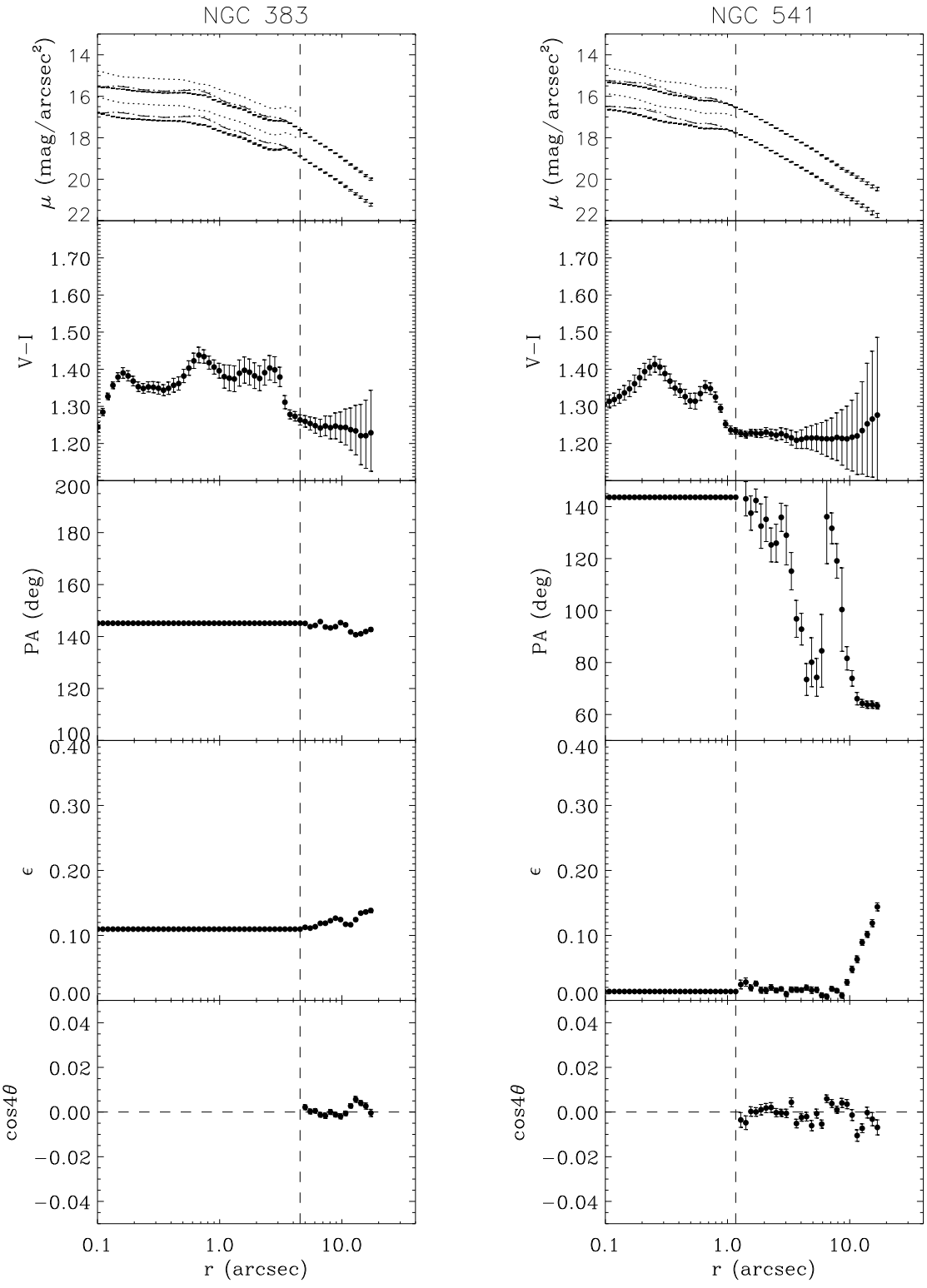

Fig. 2.— *Continued.*

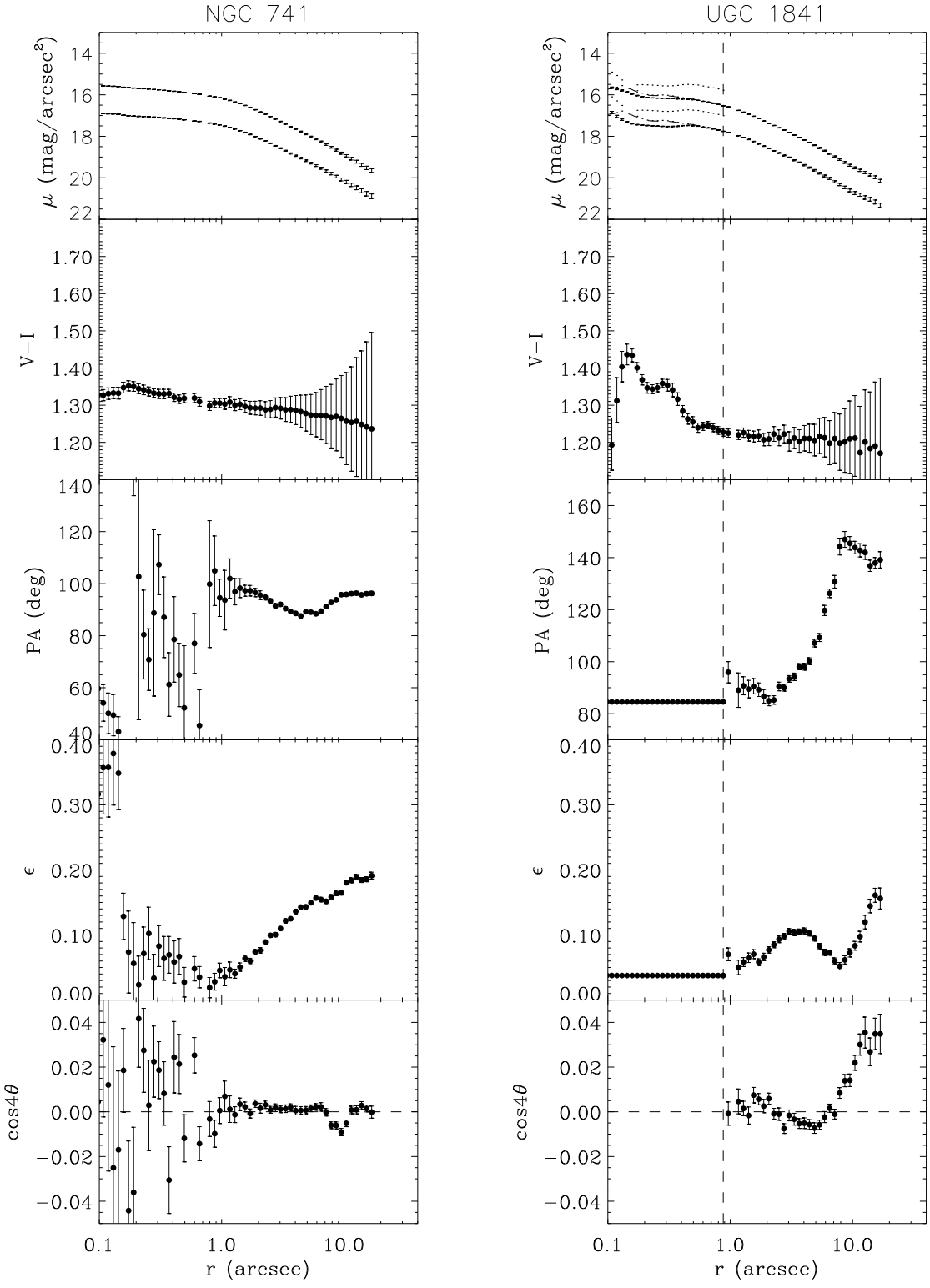

Fig. 2.— *Continued.*

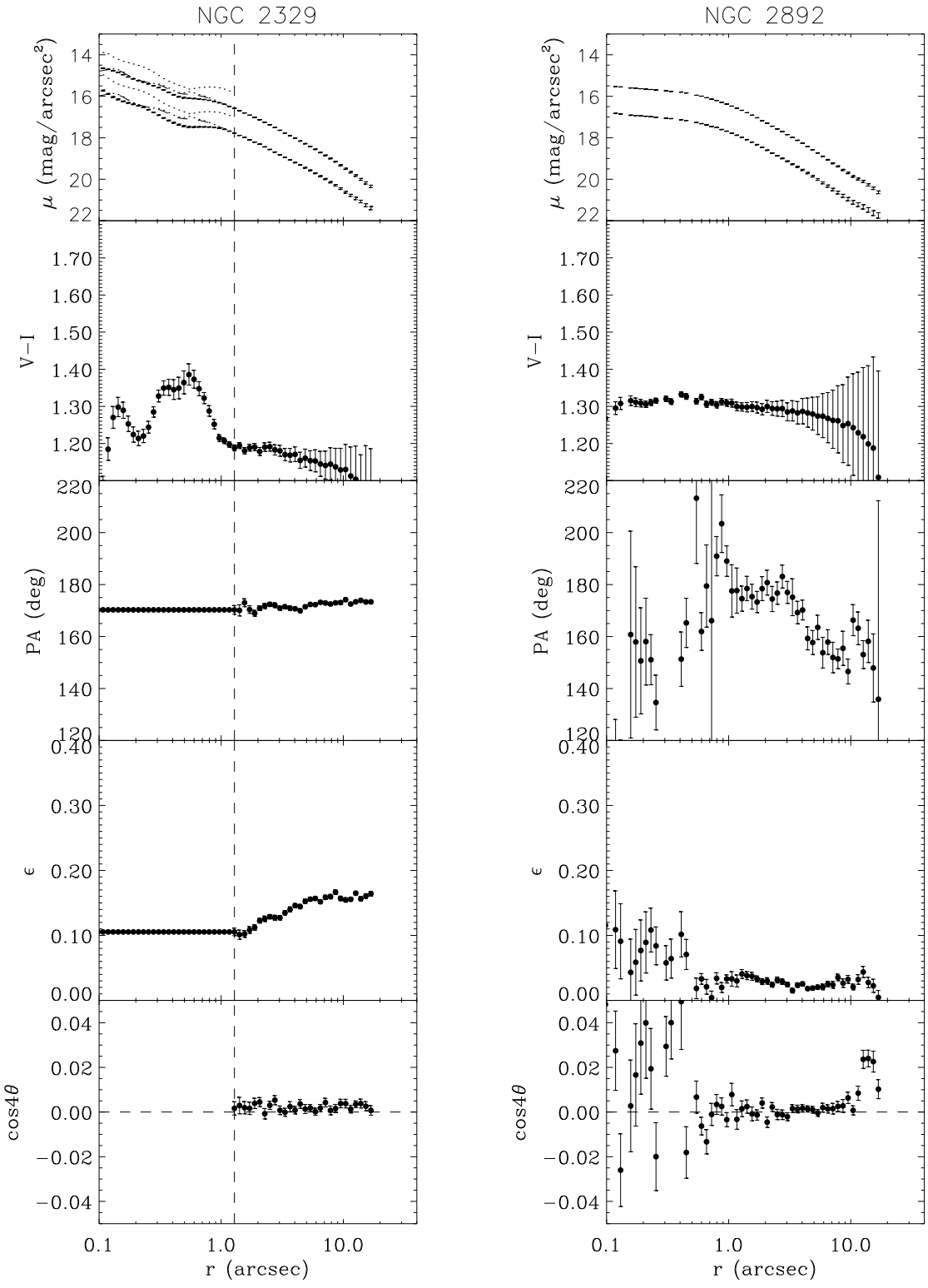

Fig. 2.— *Continued.*

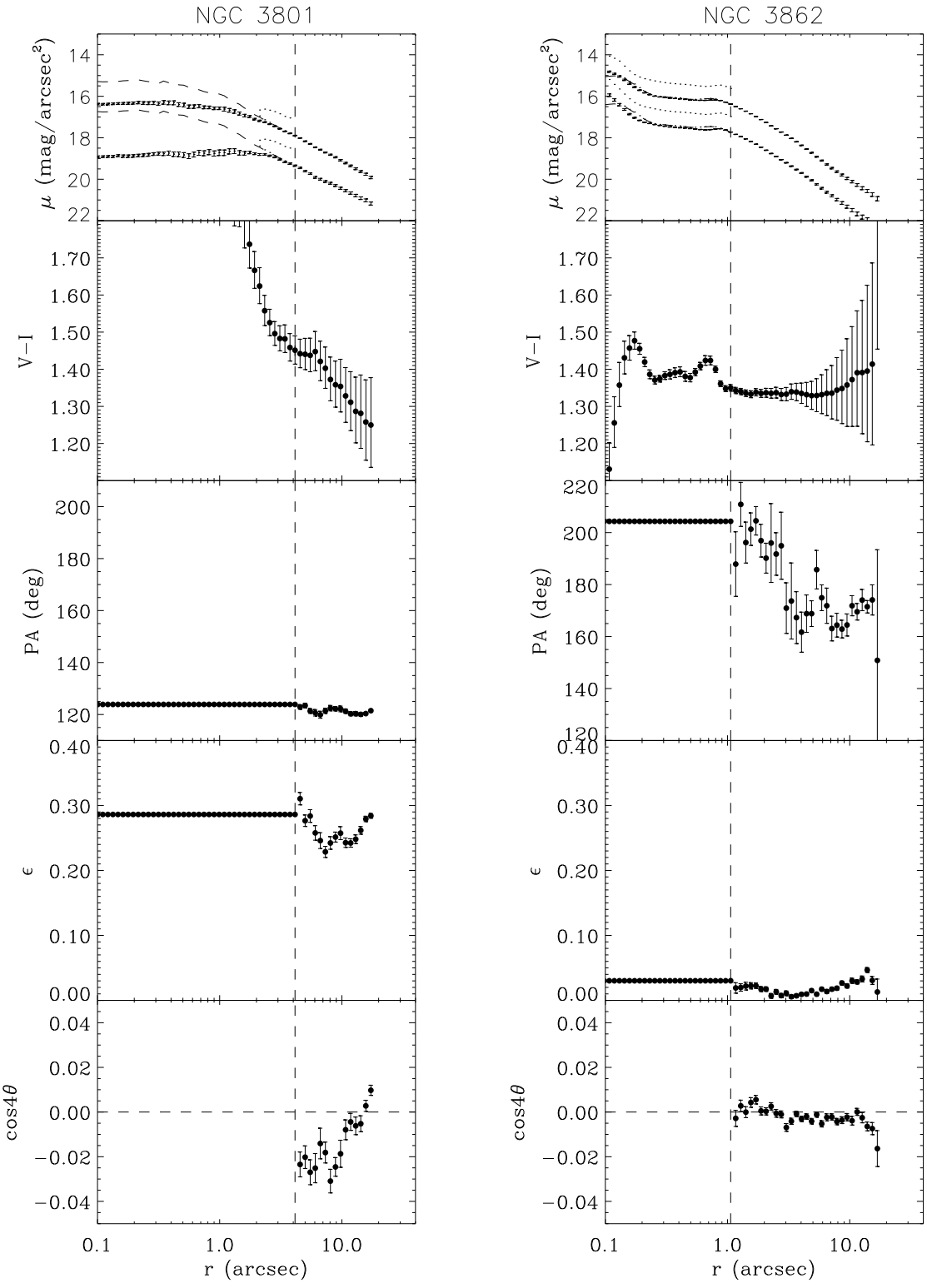

Fig. 2.— *Continued.*

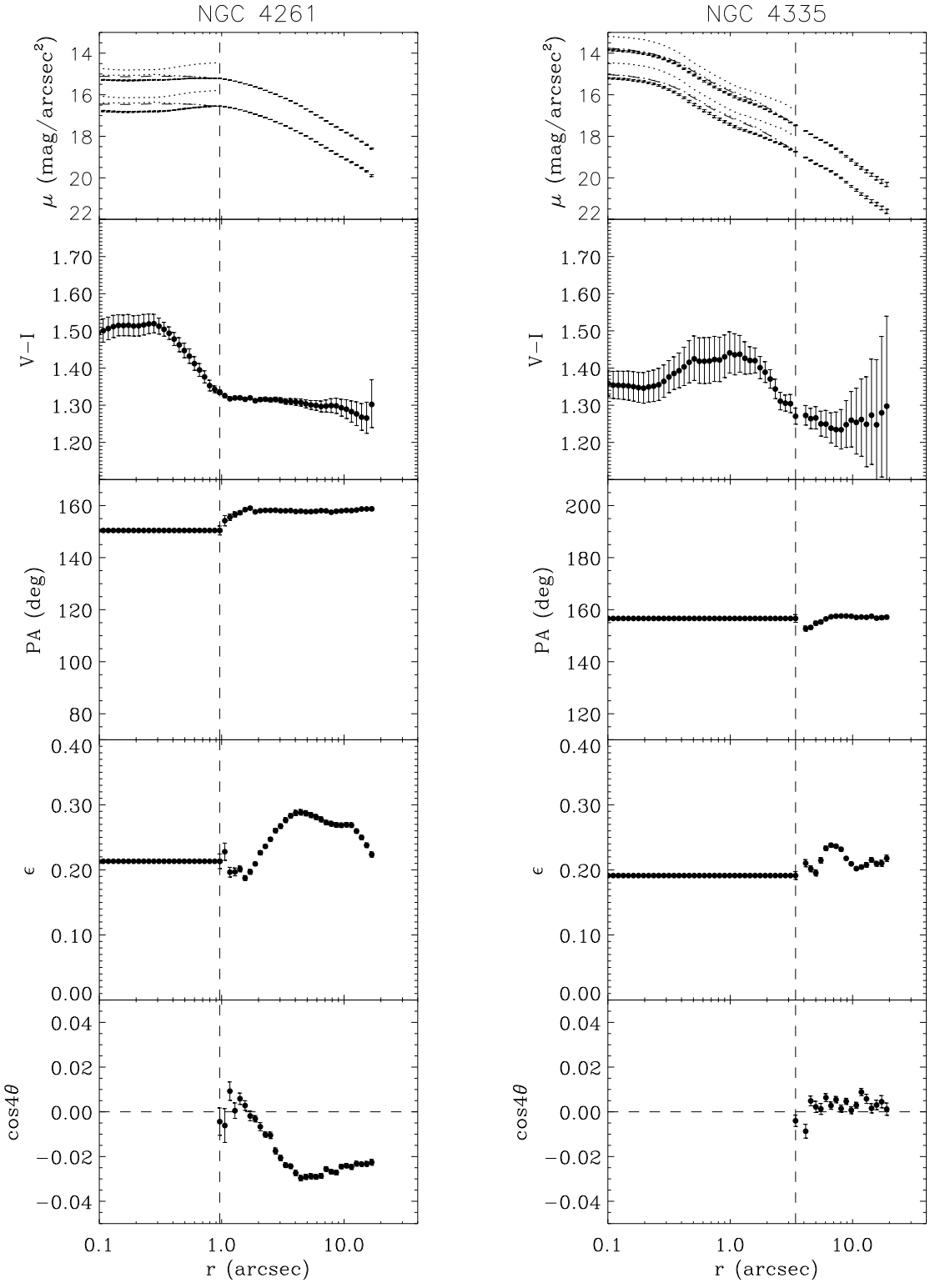

Fig. 2.— *Continued.*

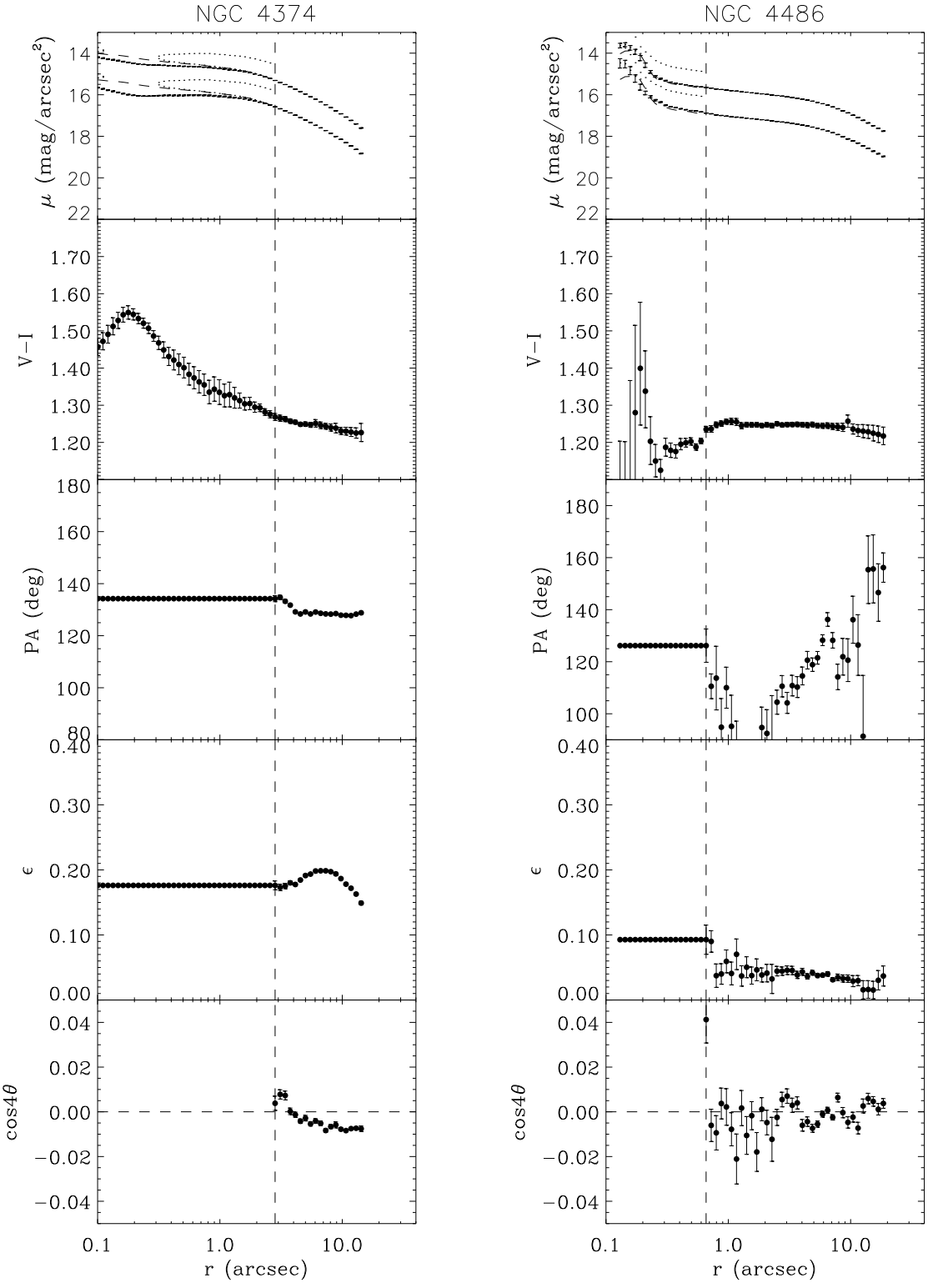

Fig. 2.— *Continued.*

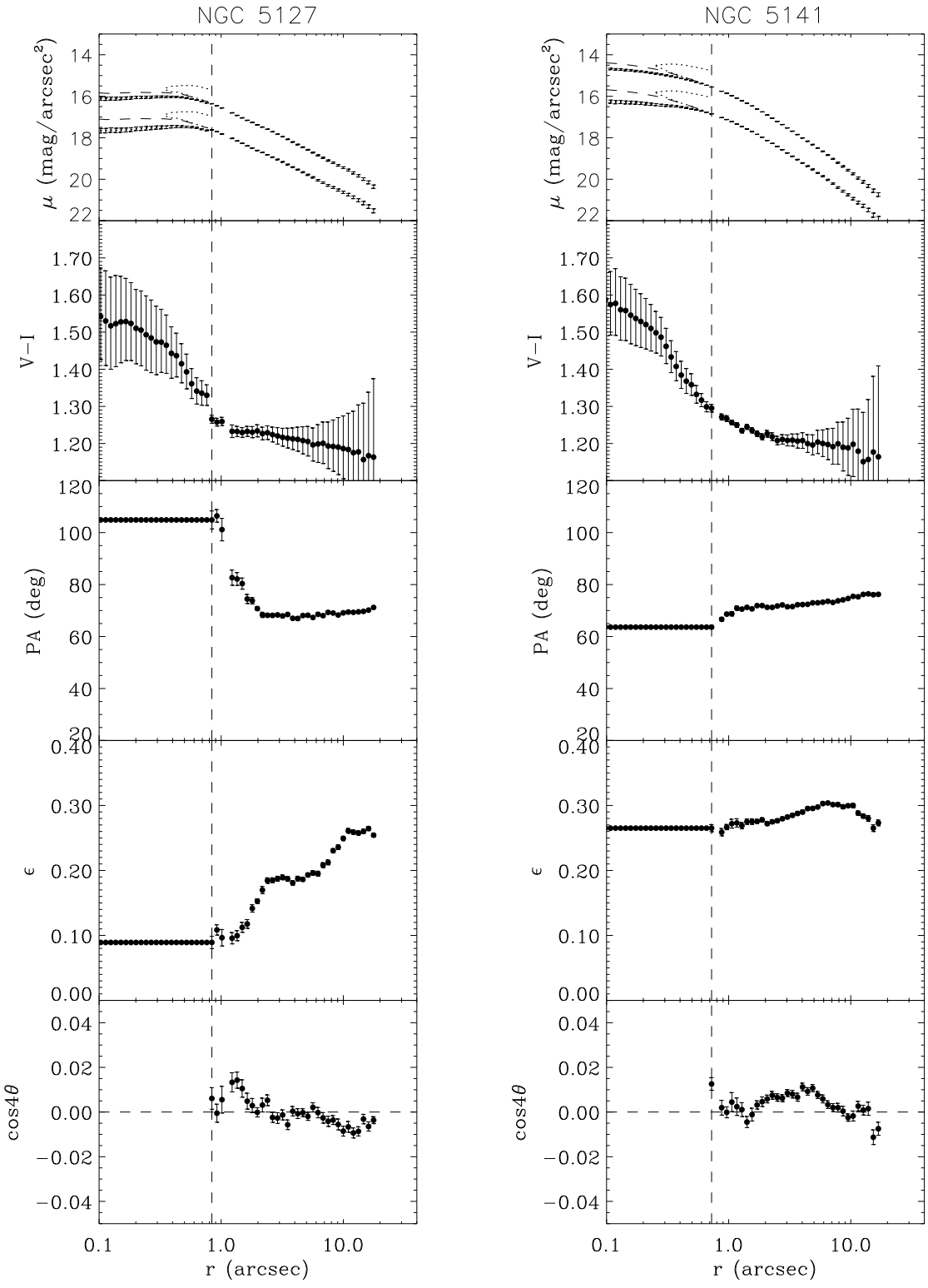

Fig. 2.— *Continued.*

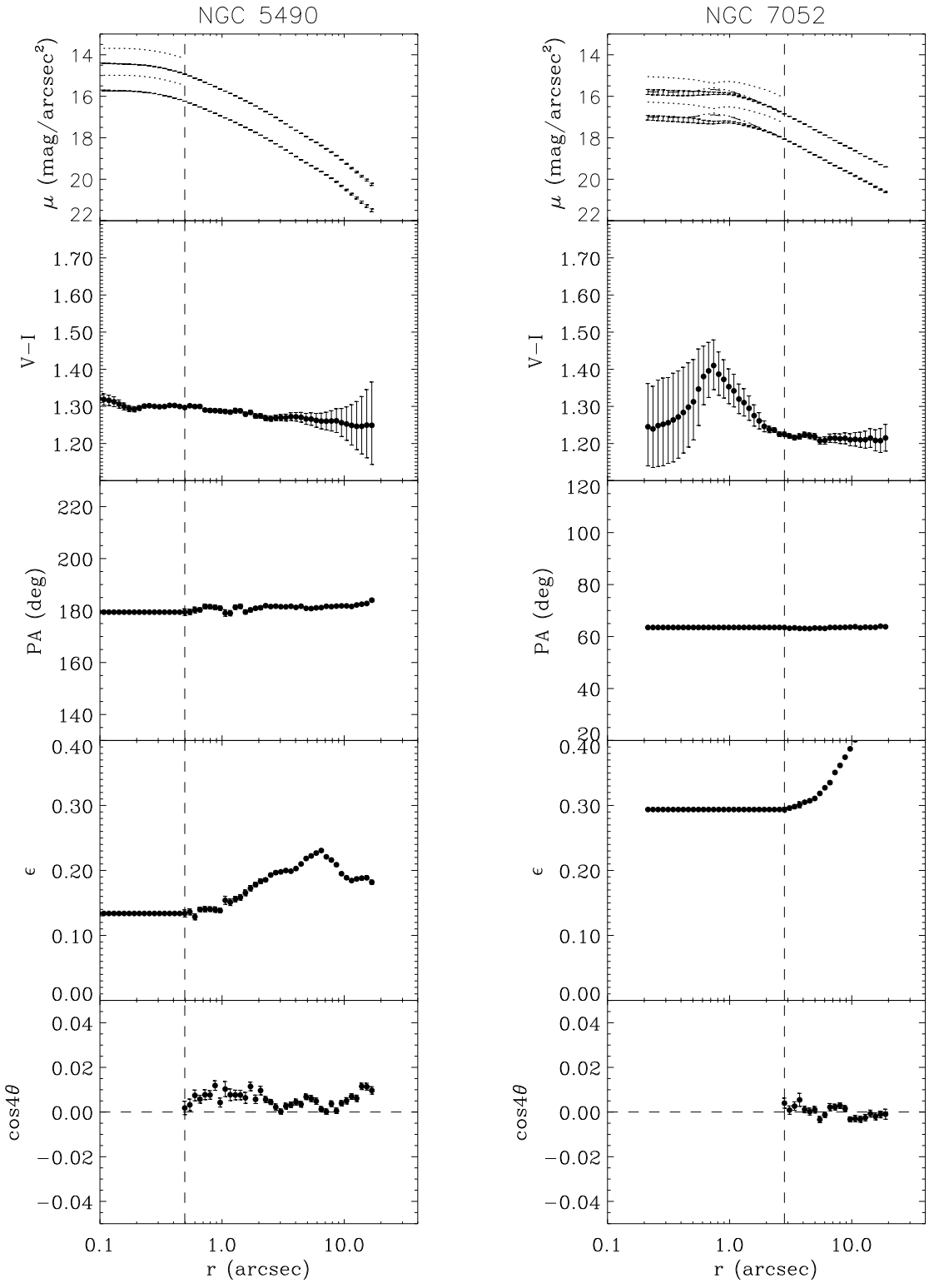

Fig. 2.— *Continued.*

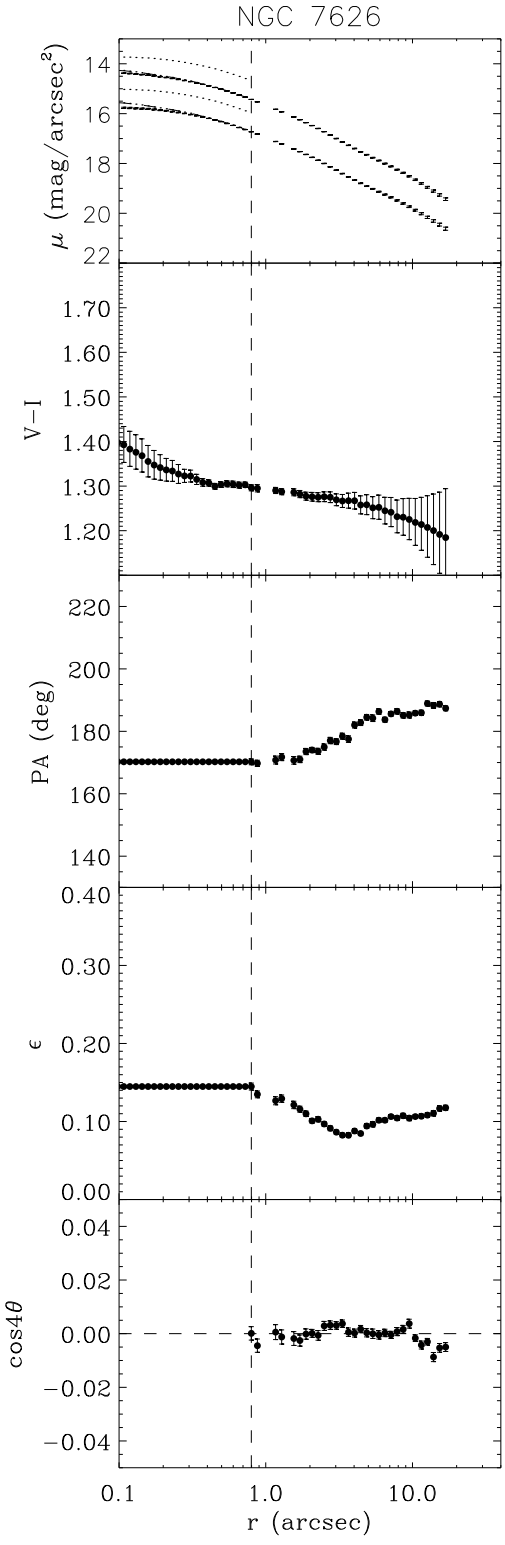

Fig. 2.— *Continued.*

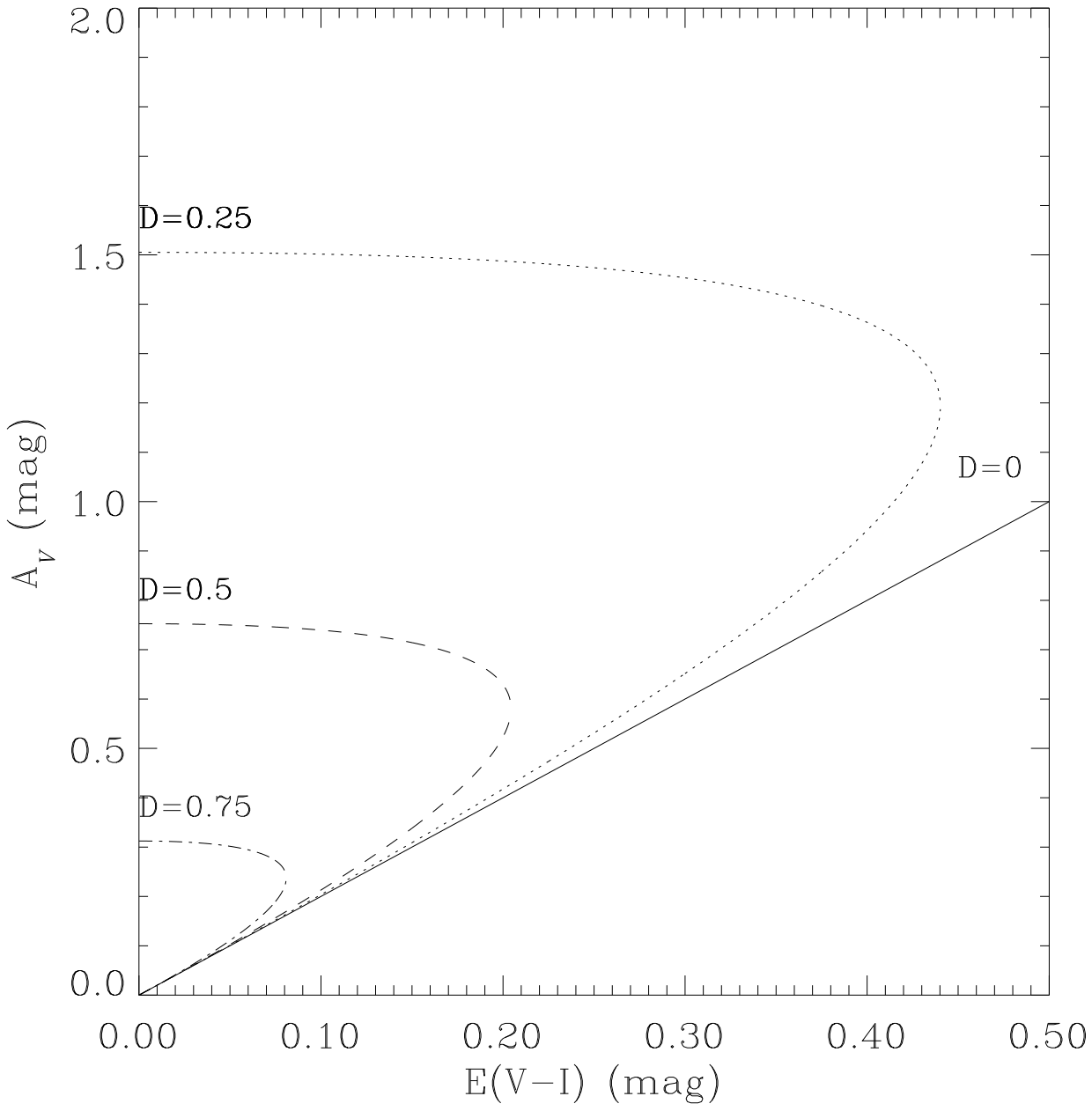

Fig. 3.— The extinction in V magnitudes due to obscuration by dust as function of observed color-excess assuming a dust screen as described in Section 3.2. Each curve gives the relation for a fixed fraction D. For a given D the maximum extinction is $2.5\log(D^{-1})$. Thus for large optical depths the magnitude correction increases with decreasing D for a given color-excess.

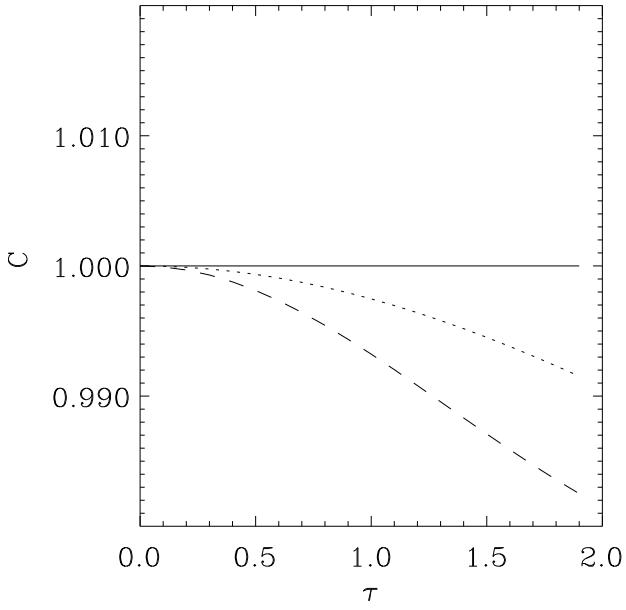

Fig. 4.— 'Total extinction factor' C (see Sec. 4.1) versus optical depth. The solid line applies for a front screen, the dashed line for a halfway screen position, i.e. with 50% of the light arising in front and behind the screen. The dotted line applies if dust and stars are homogeneously mixed.

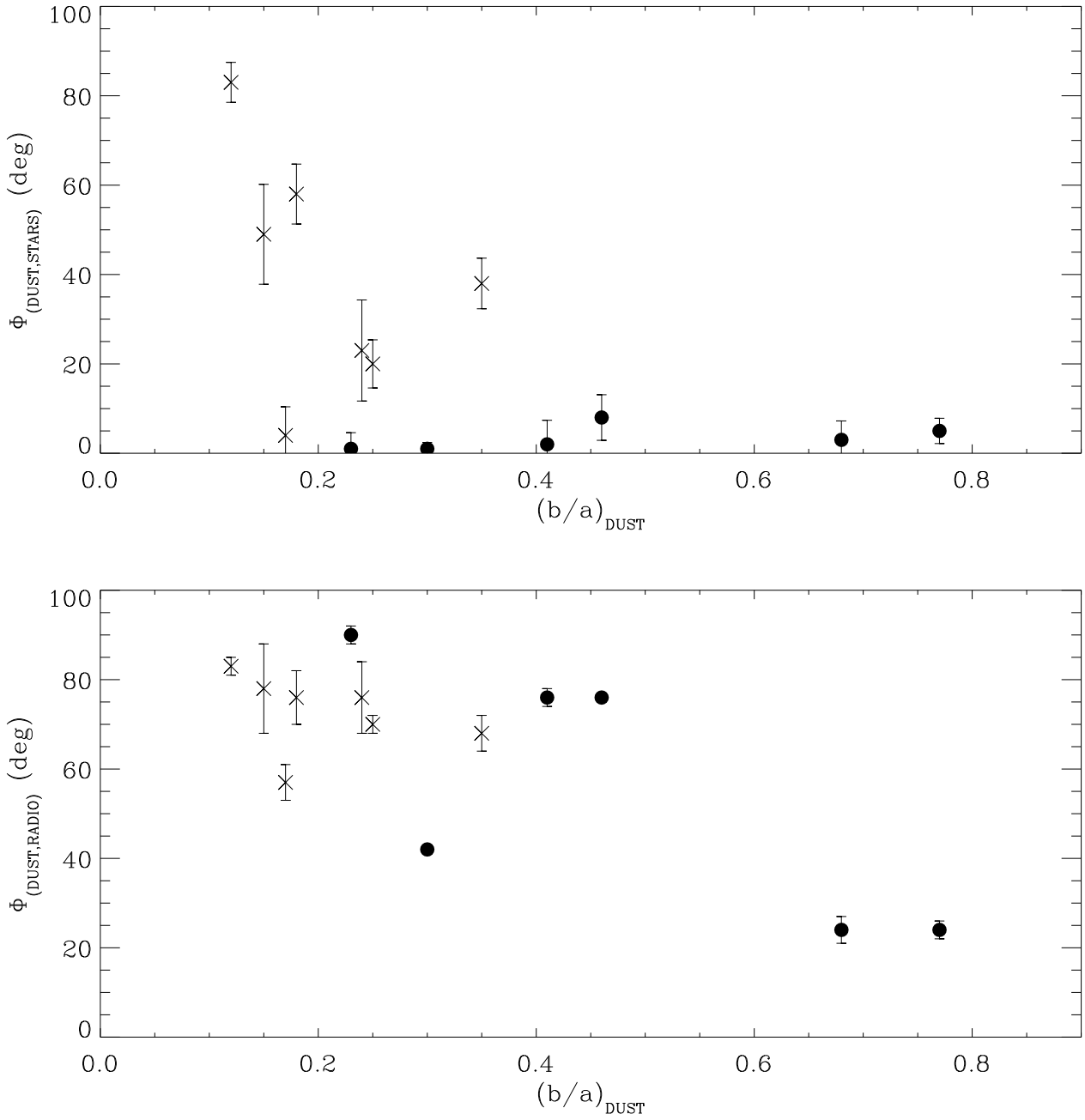

Fig. 5.— Top: relative apparent angle between dust major axis and galaxy major axis as function of the ratio of dust minor and major axis. Bottom: relative apparent angle between dust major axis dust and radio-jet axis at arcsec scale as function of the ratio of dust minor and major axis.

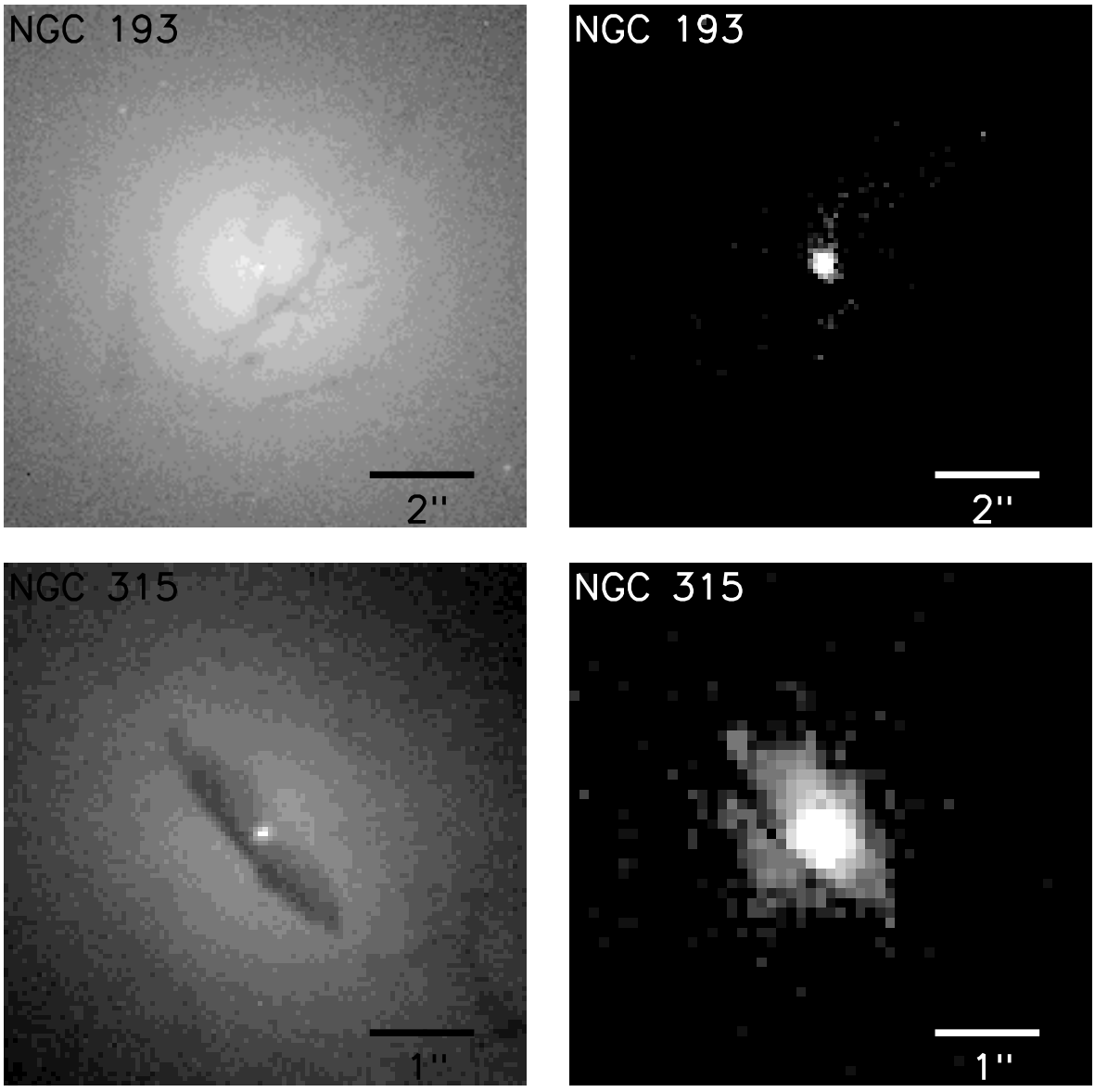

Fig. 6.— Left column are V-band images and right column are Hα+[NII] emission images. All images have logarithmic stretch. North is up and East is to the left.

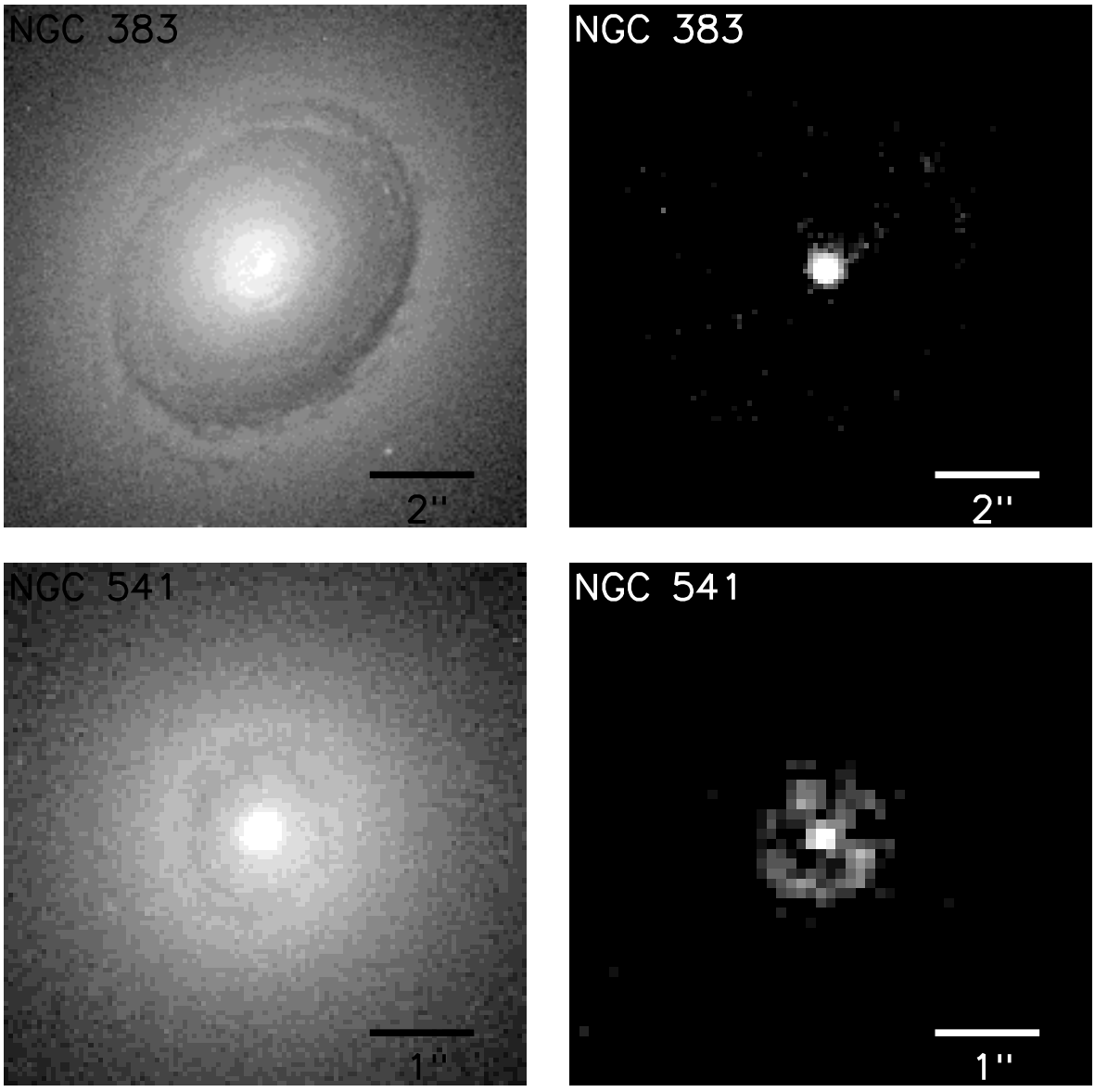

Fig. 6.— *(cont.)* Left column are V-band images and right column are Hα+[NII] emission images. All images have logarithmic stretch. North is up and East is to the left.

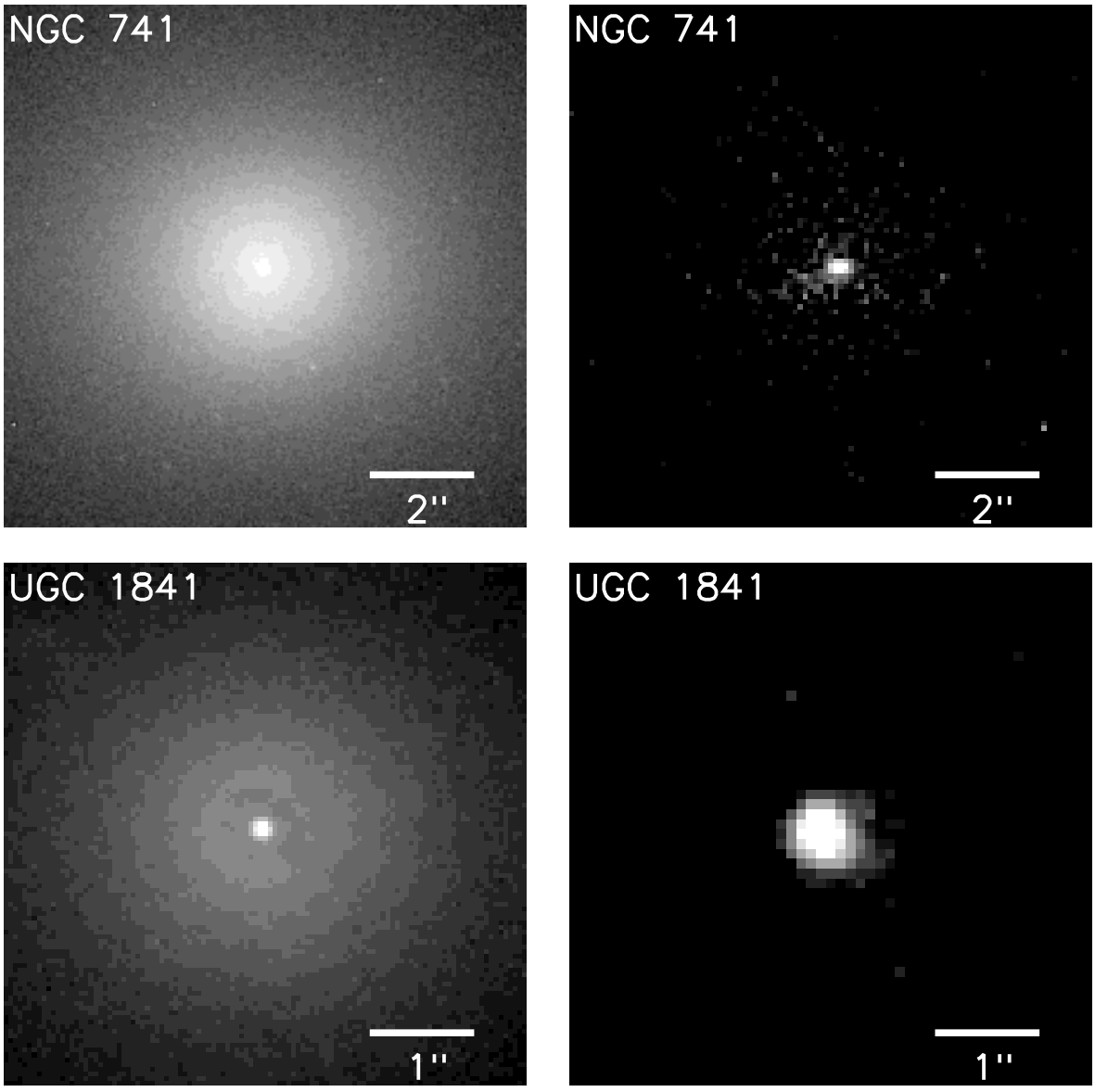

Fig. 6.— *(cont.)* Left column are V-band images and right column are Hα+[NII] emission images. All images have logarithmic stretch. North is up and East is to the left.

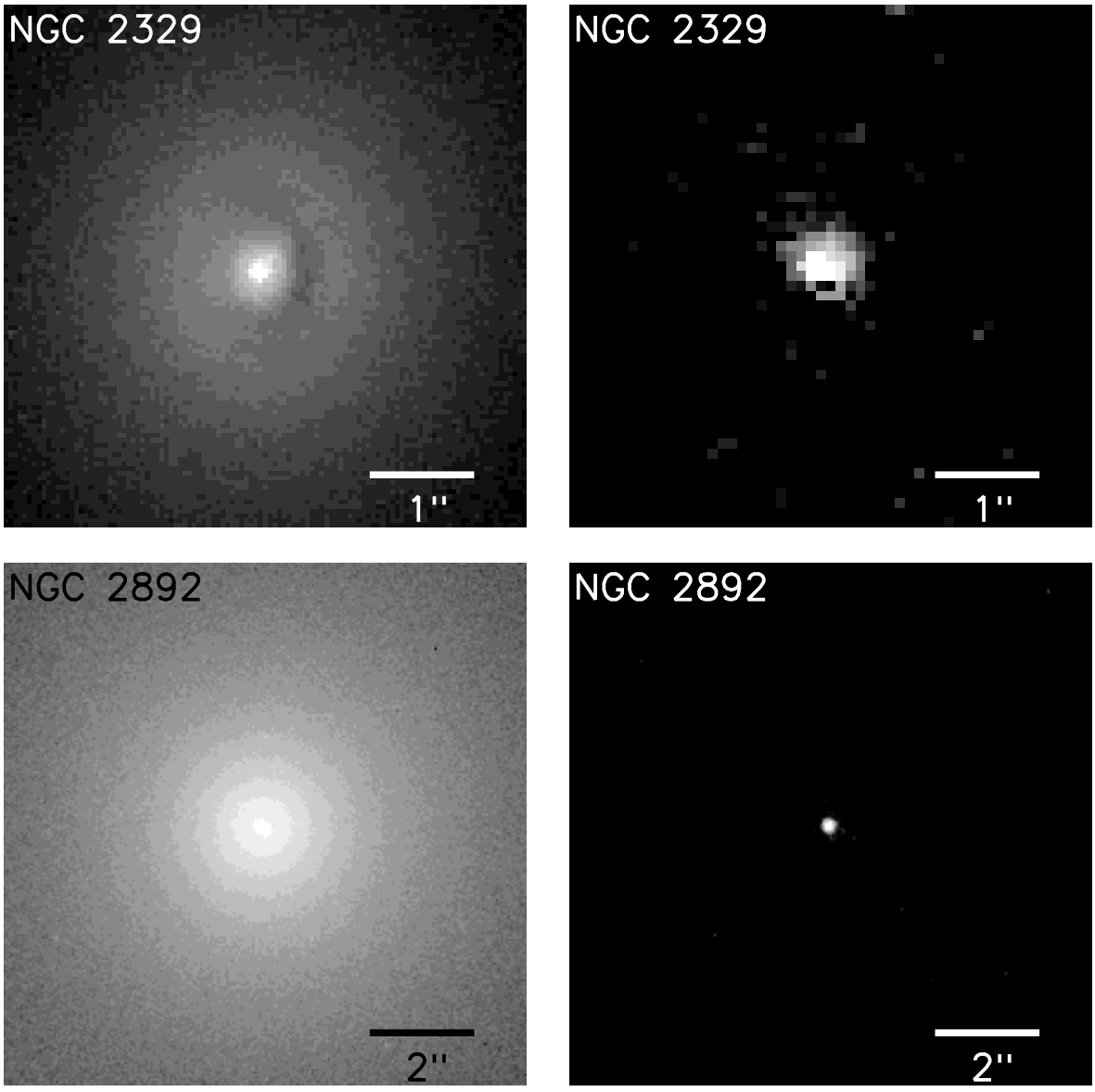

Fig. 6.— *(cont.)* Left column are V-band images and right column are Hα+[NII] emission images. All images have logarithmic stretch. North is up and East is to the left.

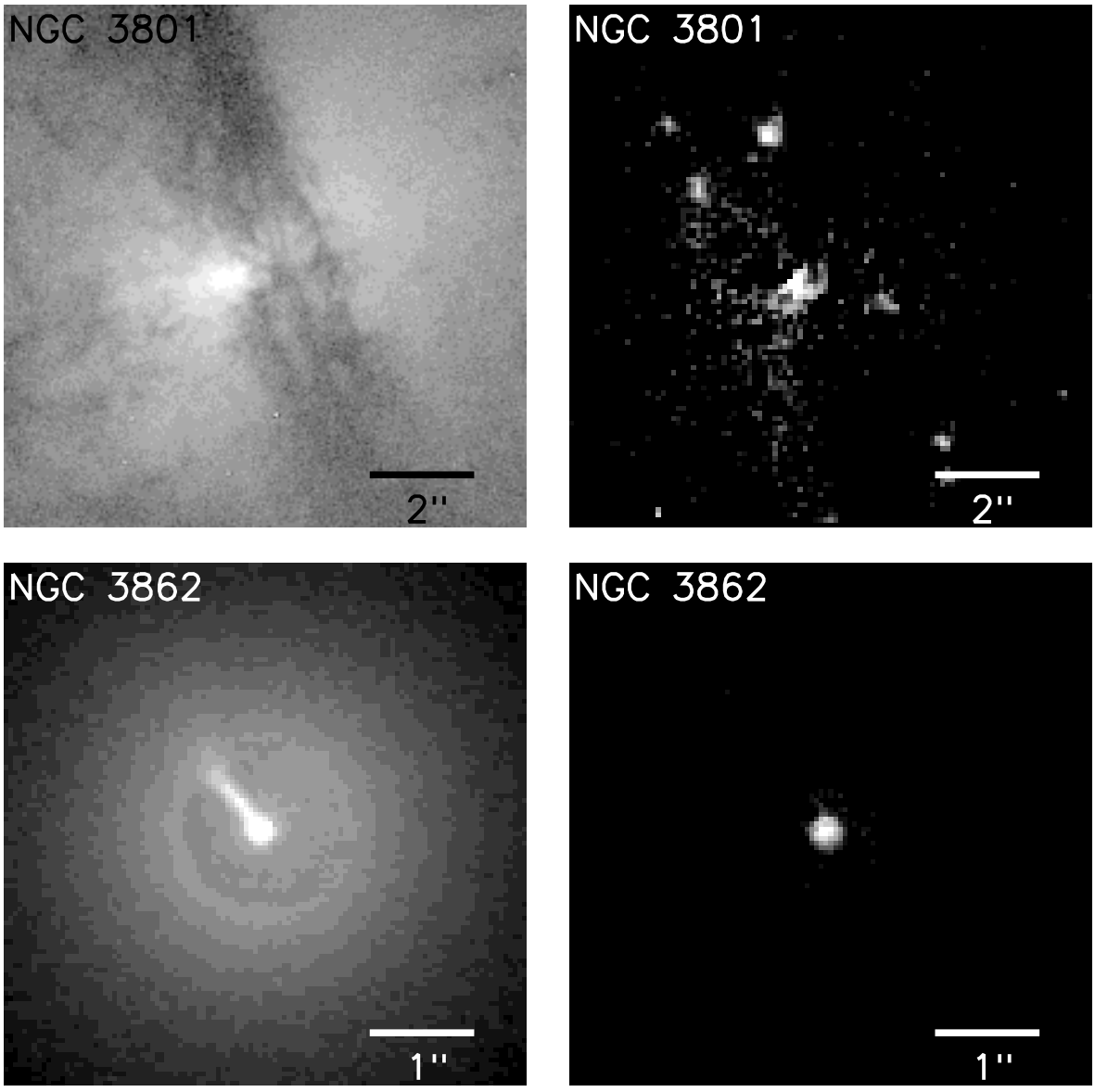

Fig. 6.— *(cont.)* Left column are V-band images and right column are Hα+[NII] emission images. All images have logarithmic stretch. North is up and East is to the left.

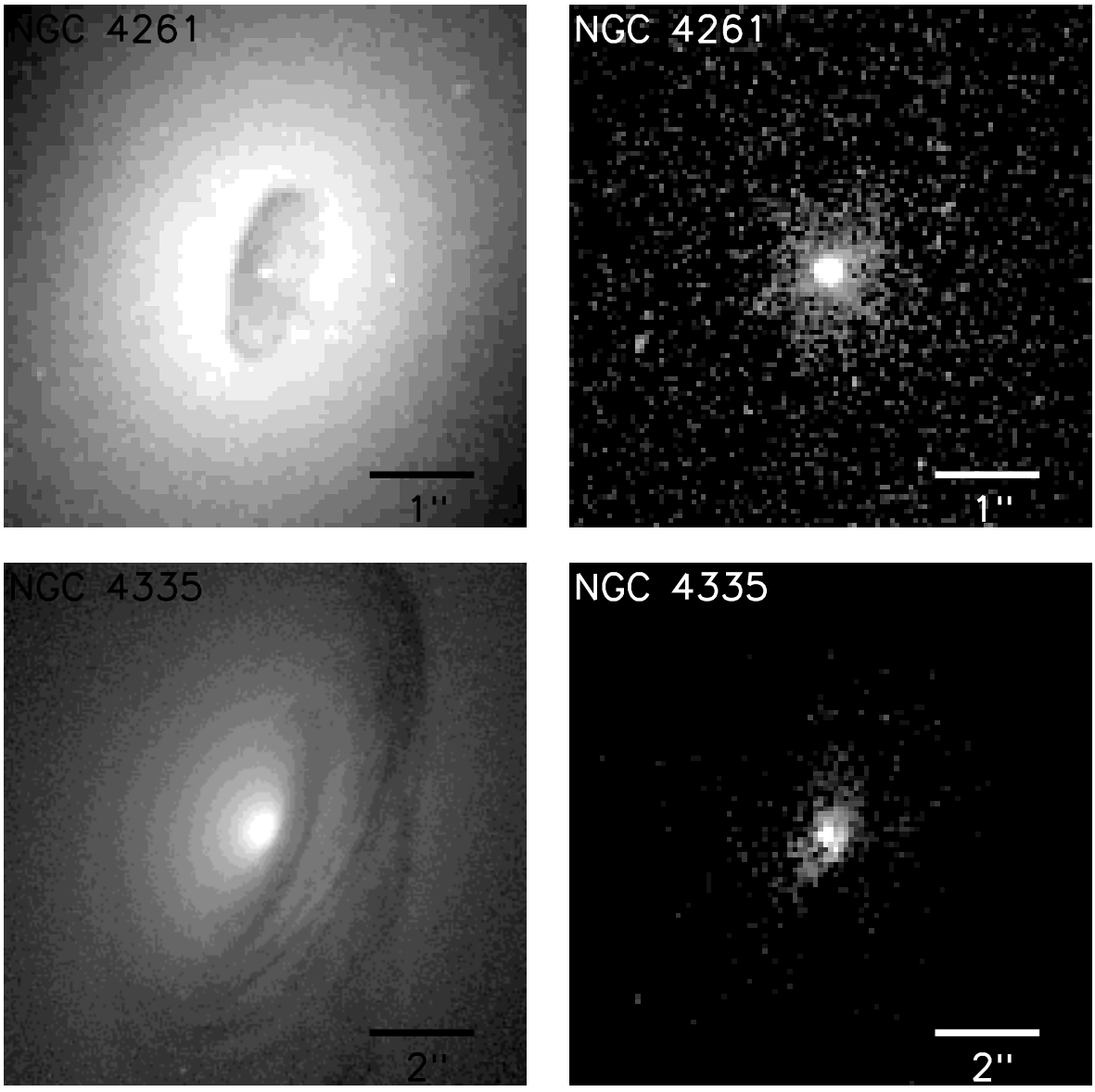

Fig. 6.— *(cont.)* Left column are V-band images and right column are Hα+[NII] emission images. All images have logarithmic stretch. North is up and East is to the left.

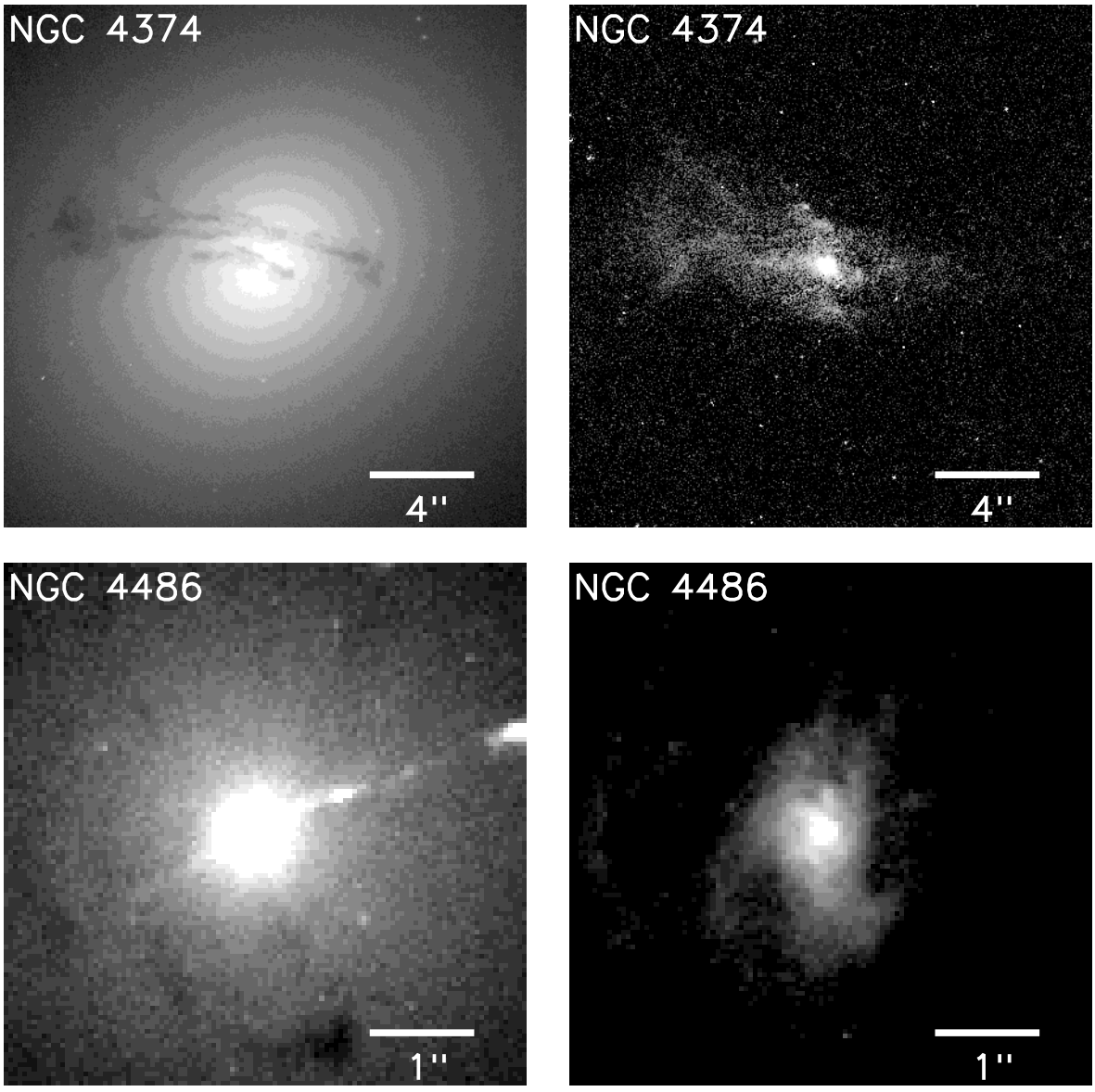

Fig. 6.— *(cont.)* Left column are V-band images and right column are Hα+[NII] emission images. All images have logarithmic stretch. North is up and East is to the left.

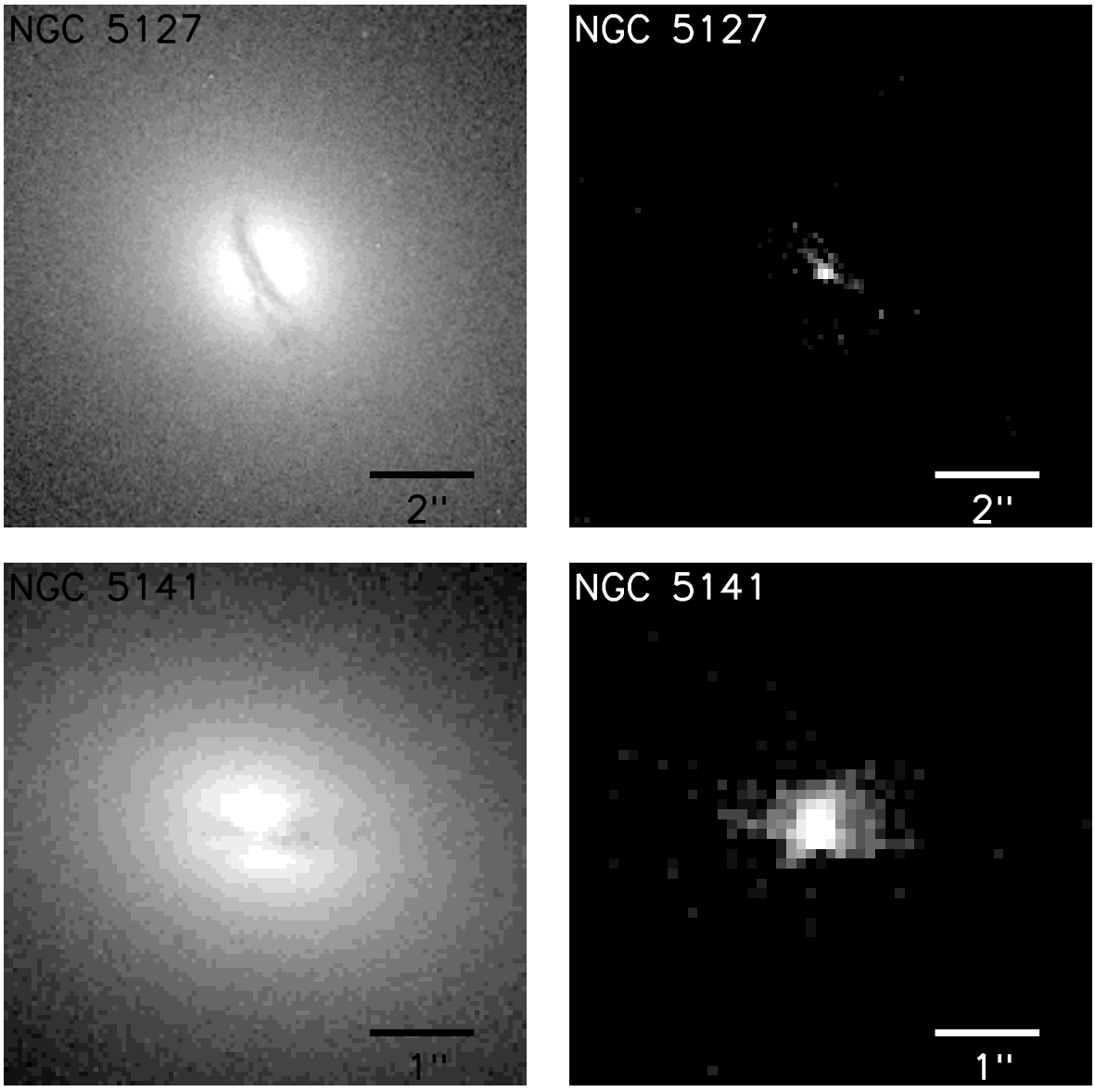

Fig. 6.— *(cont.)* Left column are V-band images and right column are Hα+[NII] emission images. All images have logarithmic stretch. North is up and East is to the left.

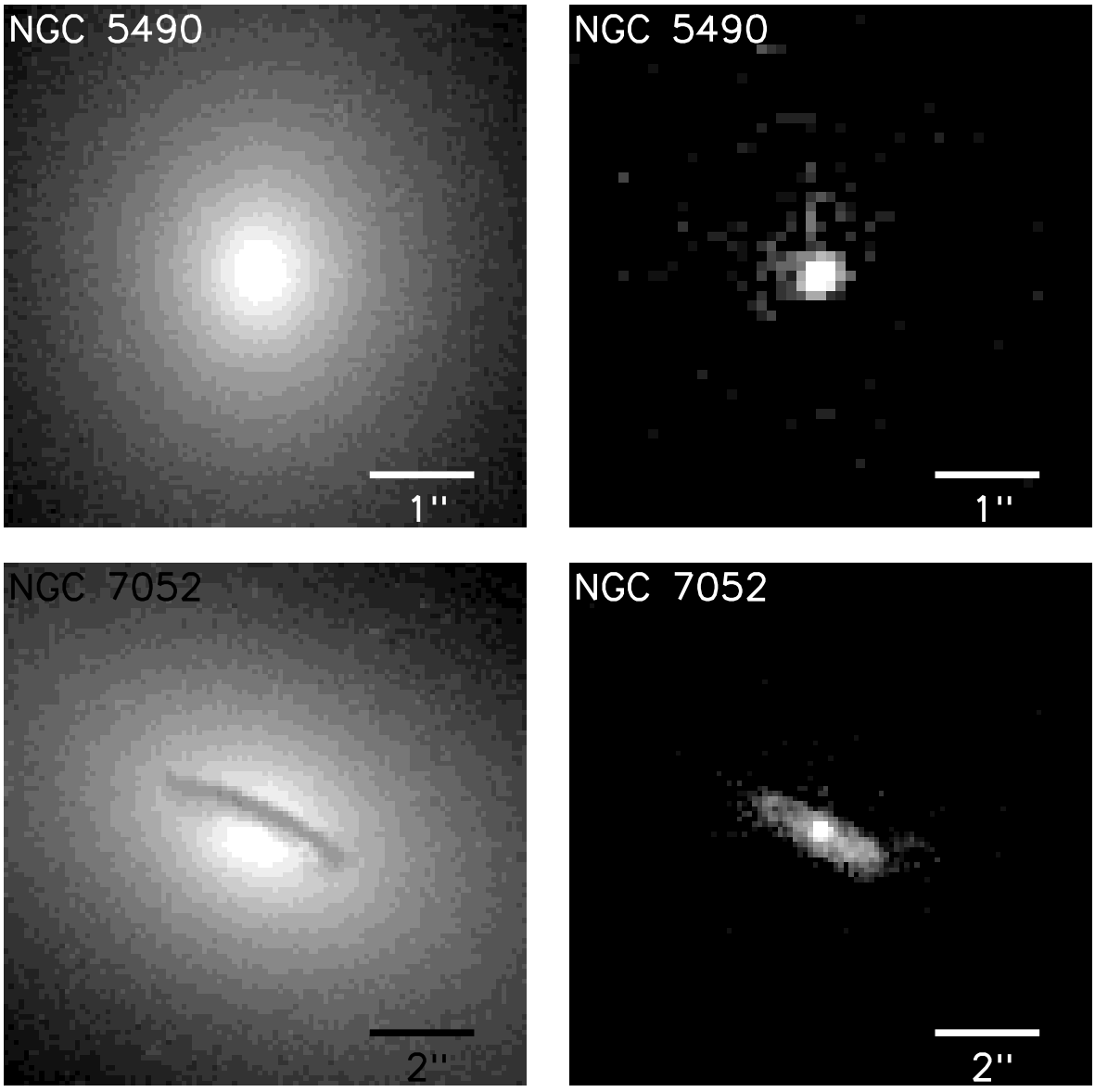

Fig. 6.— *(cont.)* Left column are V-band images and right column are Hα+[NII] emission images. All images have logarithmic stretch. North is up and East is to the left.

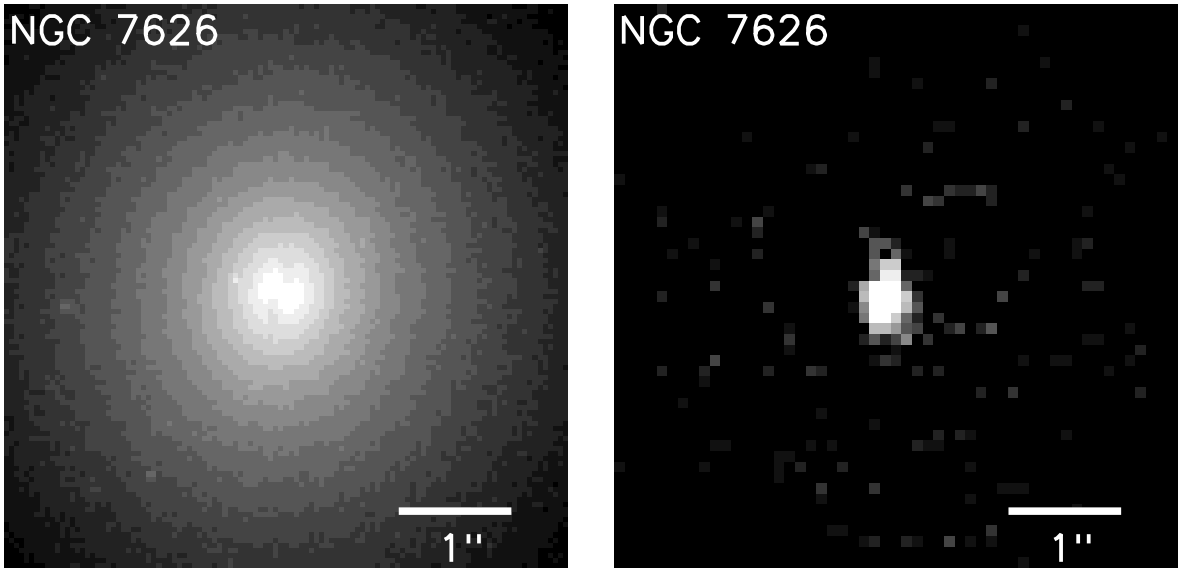

Fig. 6.— *(cont.)* Left column are V-band images and right column are Hα+[NII] emission images. All images have logarithmic stretch. North is up and East is to the left.

Table 1. Sample

NGC	UGC	Type	D_{75} (Mpc)	M_p (mag)	Log L_{radio} (WHz^{-1})	Comment
(1)	(2)	(3)	(4)	(5)	(6)	(7)
0193	00408	..	57.9	-19.9	23.84	
0315	00597	E	67.9	-21.8	24.01	
0383	00689	S0	65.2	-20.6	24.42	3C 31
0541	01004	E	73.3	-20.3	23.85	
0741	01413	E	70.2	-21.0	23.76	
....	01841	E	84.8	-19.9	24.85	3C 66B
2329	03695	E-S0	76.7	-21.0	23.67	
2892	05073	E	90.8	-20.4	23.27	
3801	06635	S0?	43.4	-19.9	23.40	
3862	06723	E	84.4	-20.6	24.66	3C 264
....	07115	E	90.5	-20.3	23.85	
4261	07360	E	29.5	-20.9	24.31	3C 270
4335	07455	E	61.5	-20.3	23.02	
4374	07494	S0	15.4	-20.6	23.26	3C 272.1, M 84
4486	07654	E	15.4	-21.0	24.81	3C 274, M 87
5127	08419	E	64.4	-20.1	23.99	
5141	08433	S0	70.7	-20.3	23.71	
5490	09058	E	69.2	-20.8	23.70	
7052	11718	E	55.4	-20.0	22.95	
....	12064	E-S0	68.3	-19.9	24.29	3C 449
7626	12531	E	46.6	-20.5	23.28	

Note. — Col. (1): NGC number. Col. (2): UGC number. Col. (3): Hubble type from CB88. Col. (4): distances from Faber et al. (1989) or if not available directly from recession velocity and H_0=75 $kms^{-1}Mpc^{-1}$. Col. (5): photographic magnitude from CB88. Col. (6): total spectral radio luminosity at 1400 MHz from CB88. Col. (7): 3C and Messier numbers.

Table 2. Observational Setup

Name	Filter	T_{exp} (s)	Filter	T_{exp} (s)	Filter	T_{exp} (s)	CCD
(1)	(2)	(3)	(4)	(5)	(6)	(7)	(8)
NGC 193	F555W	460	F814W	460	LRF680	3100	WF2
NGC 315	F555W	460	F814W	460	LRF680	3100	WF2
NGC 383	F555W	460	F814W	460	LRF680	3100	WF2
NGC 541	F555W	460	F814W	460	LEF680	3100	WF2
NGC 741	F555W	460	F814W	460	LRF680	3100	WF2
UGC 1841	F555W	460	F814W	460	LRF680	3500	WF2
NGC 2329	F555W	460	F814W	460	LRF680	3600	WF2
NGC 2892	F555W	460	F814W	460	F673N	3800	PC
NGC 3801	F555W	460	F814W	460	LRF680	3300	WF2
NGC 3862	F547M*	900	F791W*	750	F673N*	2500	PC
NGC 4261	F547M*	800	F791W*	800	F675W*	2000	PC
NGC 4335	F555W	460	F814W	460	LRF680	3600	WF2
NGC 4374	F547M*	1200	F814W*	520	F658N*	2600	PC
NGC 4486	F555W*	1200	F814W*	1200	F658N*	2700	PC
NGC 5127	F555W	460	F814W	460	LRF680	3300	WF2
NGC 5141	F555W	460	F814W	460	LRF680	3400	WF2
NGC 5490	F555W	460	F814W	460	LRF680	3300	WF2
NGC 7052	F547M*	800	F814W*	1400	LRF680*	3700	WF2
NGC 7626	F555W*	1000	F814W*	460	LRF680	5100	WF2

Note. — Col. (1): Target NGC or UGC number. Cols. (2) and (3): name and exposure time for the V band filter. Cols. (4) and (5): name and exposure time for the I band filter. Cols. (6) and (7): name and exposure time for the narrow-band filter. Depending on the redshift of the galaxy either the linear ramp filter (LRF) `FR680N` or narrow-band filters `F658` and `F673` were used in order to have the Hα+[NII] emission lines centered on the passband of the filter. NGC 4261 was observed through a broad-band filter since no narrow-band filter contained the Hα+[NII] emission lines. All observations marked with a * were not observed in our program but retrieved from the `HST` archive. Col. (8) lists the `WFPC2` CCD on which the target was positioned for the narrow-band exposure. For the LRF, which is a tunable narrow-band filter the positioning depends on the chosen central wavelength. The `PC` CCD has a FOV of approximately 36″ x 36″ and has a pixel size of 0.0455″. The `WF2` CCD has a FOV of approximately 80″ x 80″ and has a pixel size of 0.0996″. Targets were positioned on the PC CCD for all broad-band observations except one. The `F547M` observation of NGC 7052 was positioned on the WF2 CCD.

Table 3. Hα+[NII] emission properties

Name	F(< 1kpc) (10^{-14}erg/s/cm^2)	F(< 1″) (10^{-14}erg/s/cm^2)	F_{tot} (10^{-14}erg/s/cm^2)	L(< 1kpc) (10^{39} erg/s)	L(< 1″) (10^{39} erg/s)	L_{tot} (10^{39} erg/s)	$L_{lit.}$ (10^{39} erg/s)	Ref.
(1)	(2)	(3)	(4)	(5)	(6)	(7)	(8)	(9)
NGC 193	1.3	0.8	1.3	5.4	3.1	5.4		
NGC 315	4.4	3.9	4.4	24.1	21.6	24.1	26.5	1
NGC 383	2.9	2.4	3.0	14.5	12.0	15.2		
NGC 541	0.7	0.6	0.7	4.3	3.9	4.3	15.1	2
NGC 741	1.3	0.6	1.3	7.8	3.3	7.8		
UGC 1841	2.3	2.2	2.3	20.0	19.2	20.0		
NGC 2329	0.9	0.9	0.9	6.0	6.0	6.0		
NGC 2892	1.1	1.1	1.1	11.1	11.1	11.1		
NGC 3801	3.4	0.3	8.9	7.6	0.8	20.1		
NGC 3862	6.9	6.9	6.9	58.8	58.8	58.8		
NGC 4261	7.2	6.7	7.2	7.4	7.0	7.4	6.8	3
NGC 4335	0.2	0.2	0.2	0.9	0.9	0.9		
NGC 4374	29.8	7.5	29.8	8.5	2.1	8.5	6.1	4
NGC 4486	53.6	37.6	53.6	15.2	10.7	15.2	5.7	6
NGC 5127	0.6	0.3	0.6	3.2	1.3	3.2	< 8.1	5
NGC 5141	1.0	0.9	1.0	6.2	5.6	6.2	5.3	5
NGC 5490	0.7	0.7	0.7	4.2	4.2	4.2		
NGC 7052	2.6	1.9	2.6	9.4	7.0	9.4	8.7	5
NGC 7626	0.7	0.7	0.7	1.8	1.8	1.8	< 0.6	2

Note. — Col. (2): Hα+[NII] flux within a circular aperture of 1 kpc. Col. (3): Hα+[NII] flux within a circular aperture of 1″. Col. (4): total Hα+[NII] flux in image. Cols. (5)-(7): same as Col. (2)-(4) but converted to Hα+[NII] luminosities. Col. (8) total Hα+[NII] luminosities from fluxes in the literature. Col. (9): references used in Col. (8). 1: Ho et al. 1997, 2: Macchetto et al. 1996, 3: Goudfrooij et al. 1994a, 4: Bower et al. 1997, 5: Morganti et al. 1992, 6: Ford et al. 1994 (measured for $r < 1''$).

Table 4. Dust Properties

Name	Morph.	Size ($''$)	Size (pc)	Axis ratio b/a	PA_{dust} (°)	PA_{gal} (°)	PA_{radio} (°)	$M_{dust,1}$ (10^4 $M_\odot$)	$M_{dust,2}$ (10^4 $M_\odot$)
(1)	(2)	(3)	(4)	(5)	(6)	(7)	(8)	(9)	(10)
NGC 193	L	3.0	840	(0.18)	0	58	104	4	13
	I	5.4	1510						
NGC 315	D	2.5	820	0.23	40	39	130	1	3
NGC 383	D	7.4	2340	0.77	138	144	162	13	48
NGC 541	D	1.8	640	0.91	-	143	76	0.3	1
NGC 741	-	-	-	-	-	92	-	0.0	0.0
UGC 1841	D	0.8	330	~ 0.98	-	91	50	0.4	1.3
NGC 2329	D	2.0	740	0.68	174	171	150	1.4	5.3
UGC 2892	-	-	-	-	-	164	52	0.0	0.0
NGC 3801	L	21.0	4420	(0.12)	24	121	121	>42	>146
	I	60.0	12630	-	114				
NGC 3862	D	1.5	610	~ 0.99	-	25	30	0.5	1.5
NGC 4261	D	1.7	240	0.46	163	155	87	0.2	0.6
NGC 4335	D	2.5	750	0.41	158	156	82	18	58.2
	I	13.5	4030						
NGC 4374	L	13.1	980	(0.15)	79	128	1	0.3	1.0
NGC 4486	I	11.0	560	-	-	128	112	0.1	0.3
NGC 5127	L	3.0	940	(0.25)	48	68	118	1.6	6.1
NGC 5141	L	2.3	550	(0.25)	88	65	12	0.8	2.6
NGC 5490	L(D?)	0.5	170	(0.35)	143	1	75	<0.1	<0.2
NGC 7052	D	4.0	1080	0.30	65	64	23	1.5	4.8
NGC 7626	L	1.0	230	(0.17)	167	171	44	<0.1	<0.2

Note. — Col. (1): NGC / UGC number. Col. (2): morphology of dust feature; D=disk, L=lane, I=irregular. Col. (3-4): angular and physical length and diameter of lane and disk respectively. For NGC 193, NGC 3801 and NGC 4335 we give the size of both the central lanes or disk and the large dust filaments. Col. (5): Ratio of the minor and major axis of the disks. Values in parentheses give the ratio of width and length of the dust lanes. Col. (6-8): the position angles of the major axis of the dust, of the galaxy major axis just outside the central dust distribution and of the radio jet axis at arcsecond scale or smaller. Col. (9): dust mass assuming a front screen of dust. Col. (10): dust mass assuming a screen of dust half way in the galaxy.